

THE 21CM “OUTER ARM” AND THE OUTER-GALAXY HIGH-VELOCITY CLOUDS: CONNECTED BY KINEMATICS, METALLICITY, AND DISTANCE¹

TODD M. TRIPP AND LIMIN SONG

Department of Astronomy, University of Massachusetts, Amherst, MA 01003

Accepted for publication in the Astrophysical Journal

ABSTRACT

Using high-resolution ultraviolet spectra obtained with the *HST* Space Telescope Imaging Spectrograph (STIS) and the *Far Ultraviolet Spectroscopic Explorer*, we study the metallicity, kinematics, and distance of the gaseous “Outer Arm” (OA) and the high-velocity clouds (HVCs) in the outer Galaxy. We detect the OA in a variety of absorption lines toward two QSOs, H1821+643 and HS0624+6907. We search for OA absorption toward eight Galactic stars and detect it in one case, which constrains the OA Galactocentric radius to $9 < R_G < 18$ kpc. We also detect HVC Complex G, which is projected near the OA at a similar velocity, in absorption toward two stars; Complex G is therefore in the same region at $R_G = 8 - 10$ kpc. HVC Complex C is known to be at a similar Galactocentric radius. Toward H1821+643, the low-ionization absorption lines are composed of multiple narrow components, indicating the presence of several cold clouds and rapid cooling and fragmentation. Some of the highly ionized gas is also surprisingly cool. Accounting for ionization corrections, we find that the OA metallicity is $Z = 0.2 - 0.5Z_\odot$, but nitrogen is underabundant and some species are possibly mildly depleted by dust. The similarity of the OA metallicity, Galactocentric location, and kinematics to those of the adjacent outer-Galaxy HVCs, including high velocities that are not consistent with Galactic rotation, suggests that the OA and outer-Galaxy HVCs could have a common origin.

Subject headings: Galaxies:ISM — ISM: abundances — quasars: absorption lines — quasars: individual (H1821+643, HS0624+6907)

1. INTRODUCTION

Absorption-line measurements of metal abundances, physical conditions, and kinematics of diffuse gas in well-constrained locations of the outer Milky Way (e.g., Savage et al. 1995) are relatively rare, particularly near the plane of the Galaxy (Wakker 2001). Such measurements can provide unique insights into galaxy evolution for several related reasons:

First, the chemical enrichment patterns at large Galactocentric distances, and the corresponding implications regarding the Galactic abundance gradient, are fundamental observables that can be compared to theory in order to understand a variety of processes that affect the evolution of a galaxy (e.g., Chiappini et al. 2001; Carigi et al. 2005). For example, the processes by which galaxies acquire gas and fuel new star formation are not entirely understood, and this has become a key question in current galaxy evolution studies. Recent theoretical work has indicated that gas accretion might not occur through a spherical accretion shock as traditionally envisioned but instead could occur in a “cold mode” in which the matter flows into galaxies in filaments that radiatively cool and never approach the virial temperature (Katz et al. 2003; Kereš et al. 2005, 2009; Birnboim & Dekel 2003). To test models of gas accretion, it is necessary to measure the properties of incoming mat-

ter in various locations. Some of the models indicate that accreting matter can have substantial angular momentum and could settle into the outer disk (e.g., Kereš et al. 2005), a hypothesis that has some support from recent observations (Moran et al. 2012). In this case, it is also important to probe how the incoming gas is transported into the inner disk to enable new star formation or even central black hole growth and activity (Hopkins & Quataert 2010). Conversely, star formation can generate galactic fountain *outflows* that remove enriched matter from the inner galaxy. Some of outflowing material could escape entirely, but it is also probable that some of this enriched matter will return to the outer disk and add to the matter reservoir for subsequent star formation (e.g., Bregman 1980; Oppenheimer et al. 2010; Lehner & Howk 2011). These competing inflow and outflow processes should have significantly different abundance signatures: inflowing intergalactic matter should have relatively low metallicity while the outflowing fountain material is expected to be metal enriched, and indeed, low-redshift observations have shown that halo gas can be remarkably metal-poor (e.g., Tripp et al. 2005; Ribaldo et al. 2011) as well as highly enriched (e.g., Jenkins et al. 2005; Prochaska & Hennawi 2009; Tripp et al. 2011). Thus, these flows should have opposite effects on galactic abundance gradients, and ultimately a complete galactic evolution model should be able to explain observed metallicities in both the inner and outer regions of a galaxy. Similarly, it is important to constrain the microphysics of inflowing/outflowing matter – how (and where) are the flows ionized, ablated, and mixed into the general ISM? How do they subsequently cool to reach conditions suitable for new star formation? Some galactic wind models drive the outflows by radiative pres-

Electronic address: tripp@astro.umass.edu

¹ Based on observations with (1) the NASA/ESA *Hubble Space Telescope*, obtained at the Space Telescope Science Institute, which is operated by the Association of Universities for Research in Astronomy, Inc., under NASA contract NAS 5-26555, and (2) the NASA-CNES/ESA *Far Ultraviolet Spectroscopic Explorer* mission, operated by Johns Hopkins University, supported by NASA contract NAS 5-32985.

sure and may require significant quantities of dust in the outflowing material (Aguirre et al. 2001; Murray et al. 2011). Absorption-line measurements can reveal the presence of dust in the outer galaxy through abundance patterns indicative of depletion onto dust grains (e.g., Savage & Sembach 1996; Jenkins 2009), so outer-galaxy absorption studies can also shed insight on the roles played by dust in inflows and outflows.

Second, absorption-line observations of damped Ly α absorbers [DLAs; QSO absorbers with $N(\text{H I}) > 2 \times 10^{20} \text{ cm}^{-2}$] and sub-DLAs ($1 \times 10^{19} \lesssim N(\text{H I}) \leq 2 \times 10^{20}$] provide sensitive probes of the chemical enrichment history of the Universe from $z = 0$ to $z > 4$ (e.g., Prochaska et al. 2003; Wolfe et al. 2005; Meiring et al. 2009, 2011), but the context of the DLAs (i.e., the environment and nature of the absorbers) is generally hard to study, and currently only limited information is available regarding the origins of DLAs (e.g., Chen & Lanzetta 2003; Rao et al. 2003; Battisti et al. 2012). Considering the cross section of a disk or halo of gas, it is likely that many of the DLAs arise in the outer regions of galaxies. The Milky Way is a damped Ly α absorber. Since its absorption context can be scrutinized in great detail, the Milky Way provides a valuable laboratory for understanding the nature of DLAs/sub-DLAs, but measurements of abundance patterns in the more distant *outer* Galaxy are still relatively limited.

Third, while some abundances in the outer galaxy and abundance gradients have been measured using H II region emission lines, there has long been concern about whether H II region abundances are biased by “self pollution”, i.e. whether the abundances are boosted by freshly formed metals from massive stars embedded within the H II region. Abundances from absorption lines in distant background objects probe random locations with respect to foreground H II regions and can test the self-pollution hypothesis, and some absorption-line studies have indeed suggested that self pollution does occur (Cannon et al. 2005 and references therein). The discovery that many gas-rich galaxies have “extended ultraviolet disks” (Thilker et al. 2007) underscores the importance of investigating this issue – H II regions may be biased in favor of the UV-bright star clusters that comprise the extended UV disks and might not accurately represent abundance gradients for testing theoretical work as discussed above.

Fourth, outer galaxy abundances can be used to investigate whether some gaseous structures of the Milky Way could be due to interactions with satellite galaxies. This is related to the questions raised above: one means to bring gas into galaxies is to strip the interstellar media of dwarf satellite galaxies as they plunge into, and merge with, the central galaxy. Satellite interactions can also stimulate the growth of galactic structures such as warps (e.g., Weinberg & Blitz 2006; Quillen et al. 2009) and may drive continuing (low-level) star formation in elliptical galaxies (Kaviraj et al. 2011). Since satellite galaxies can have significantly different abundances compared to each other and the Galactic disk, the outer galaxy abundances provide clues about the origins of galactic structures and the importance of this mechanism for bringing additional gas into galaxies.

For these reasons we have conducted a study of the abundances in the outer galaxy using absorption lines recorded in high-resolution spectra of two QSOs observed

with the *Hubble Space Telescope* (*HST*) and the *Far Ultraviolet Spectroscopic Explorer* (*FUSE*). We selected two QSOs for this study, HS0624+6907 and H1821+643. These sight lines are unique among the QSOs and AGNs that have been observed in the ultraviolet at high spectral resolution and with good signal-to-noise (S/N) ratios because the QSOs are at relatively low Galactic latitudes and thus provide an opportunity to study outer-galaxy gas near the plane. Moreover, these QSOs lie behind a high-velocity gaseous structure with a large angular extent in the outer galaxy known as the “Outer Arm” (OA). This structure is also unique because its distance has recently been constrained, which is valuable for understanding its nature and implications. In addition, there are several high-velocity cloud complexes near the OA with similar kinematics, including Complexes C, G, and H. The *HST* archive includes high-quality spectra of many stars in the directions of these gas clouds, and these stellar spectra provide an opportunity to obtain new constraints on the distance of these objects. In this paper, we present a study of these outer-Galaxy gaseous structures. We focus on the abundances and physical conditions in the Outer Arm and whether the OA is related to the HVCs in its proximity. In § 2, we provide some comments on the Outer Arm and the QSO sight lines that probe this part of the Galaxy. We present the QSO and star observations and absorption-line measurements in § 3 and § 4, respectively, and we discuss new constraints on the distance of the Outer Arm, and the nearby high-velocity cloud Complex G, in § 5. In § 6, we examine the physical conditions of the OA, and we use models to evaluate the impact of ionization corrections on the metallicity measurements. We also make some remarks on the nature of the highly ionized gas in the Outer Arm. We discuss our results in § 7 with an emphasis on the possible origin and implications of the Outer Arm.

2. QSO SIGHT LINES THROUGH THE OUTER ARM

The Outer Arm is a large, contiguous neutral hydrogen complex located in Galactic coordinates at $49^\circ \lesssim l \lesssim 180^\circ$ and $4^\circ \lesssim b \lesssim 31^\circ$ over a velocity range $-150 \lesssim v_{\text{LSR}} \lesssim -100 \text{ km s}^{-1}$. Figure 1 shows an all-sky map of high-velocity 21 cm emission from Wakker et al. (2003) including the Outer Arm. The structure has long been known from 21cm emission studies (e.g., Westervhout 1957; Kepner 1970; Burton & te Lintel Hekker 1986), and it is often interpreted to be gas in the outermost Galactic spiral arm and/or the warped region of the outer disk at a Galactocentric distance $R_G \approx 15 \text{ kpc}$ (e.g., Kepner 1970; Diplas & Savage 1991; Haud 1992). However, whether this gaseous structure is really a spiral arm has long been questioned (e.g., Davies 1972; Weaver 1974), and other hypotheses regarding the nature of this object remain viable. The OA extends to substantial latitudes (Figure 1), which implies a large z -height that may be difficult to reconcile with an origin in the Galactic warp, and in some regions it exhibits large deviations from Galactic rotation speeds (e.g., Wakker 2001) that are problematic for the spiral arm interpretation. Indeed, recently obtained constraints on the OA distance and kinematics (Lehner & Howk 2010) call into question whether this gas cloud is indeed related to the Galactic warp and outer spiral arm (see below). Moreover, the

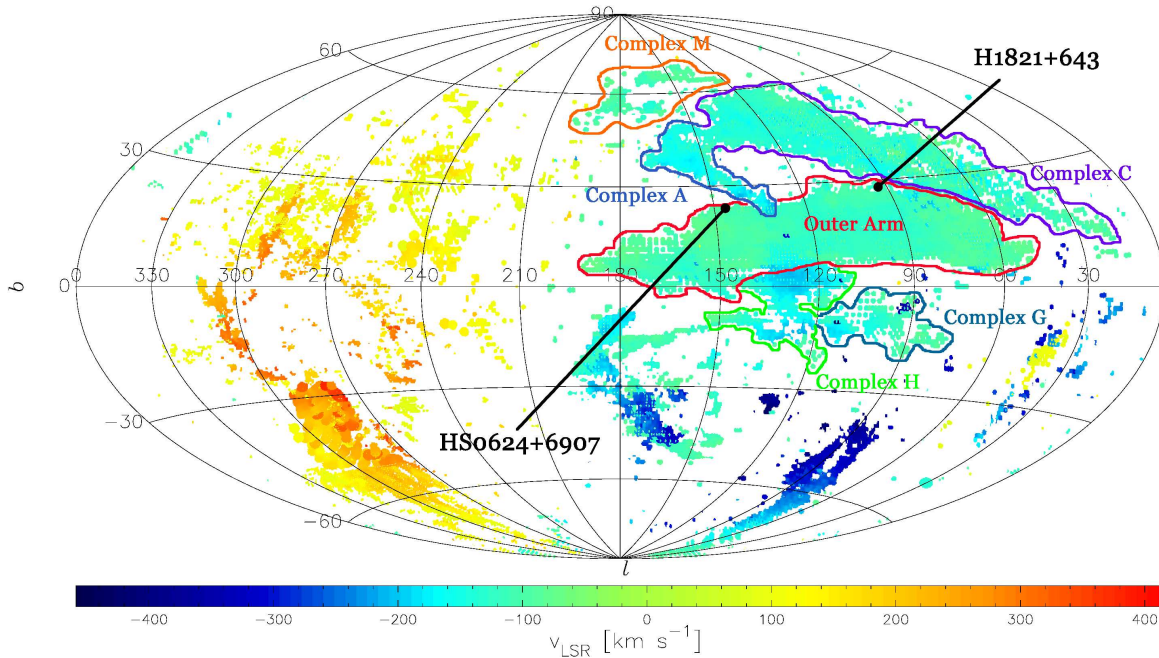


FIG. 1.— Locations of the QSO sight lines H1821+643 and HS0624+6907 with respect to the 21 cm emission from the Outer Arm. This map, from Wakker et al. (2003), shows 21 cm emission from the Galactic high-velocity clouds (HVCs) and the Outer Arm in Galactic coordinates (longitude increases from right to left along the x -axis). LSR velocities are indicated by color using the scale at the bottom of the figure, and several of the HVC complexes near the Outer Arm are labeled.

similarity of the kinematics and distance of the OA and the nearby HVCs Complex C and Complex G (see §5) suggests that the OA and Complexes C and G (and possibly H) could be related. Such a complex configuration of HVCs would not be expected in the warp/spiral arm interpretation.

The 21 cm emission from the Outer Arm is detected at velocities similar to expected velocities for a rotating Galactic disk in this general direction, and consequently, the OA is often ignored in studies of Galactic HVCs, although it is included in the HVC compendium of Wakker (2001). Recently, Lehner & Howk (2010) have used the Cosmic Origins Spectrograph (COS) on *HST* to detect the OA in ultraviolet absorption lines toward HS1914+7139 ($l = 103^\circ, b = +24^\circ$), a B2.5 IV star at an estimated Heliocentric distance of 14.9 kpc. Interestingly, *they detect OA absorption toward this star at two velocities, $v_{\text{LSR}} = -118$ and -180 km s^{-1}* . This observation places an upper limit² on the distance to the OA: the Galactocentric radius $R_G(\text{OA}) < 17.6 \text{ kpc}$. This is in agreement with the distance typically derived for the OA, assuming it is part of the Galactic warp, i.e., $R_G \approx 15 \text{ kpc}$ (Haud 1992). The OA component at $v_{\text{LSR}} = -118 \text{ km s}^{-1}$ is roughly consistent with corotation at the usually adopted OA distance, although this velocity implies that the OA should be at a Galactocentric radius that is $\approx 5 \text{ kpc}$ farther out than the R_G upper limit. The other velocity component detected by Lehner & Howk, $v_{\text{LSR}} = -180 \text{ km s}^{-1}$, is more interesting: this velocity is highly inconsistent with a rotating-disk origin; corotating disk gas would be far beyond the star at this velocity, even with the increased Milky Way rotation speed derived by Reid et al. (2009). A small portion of the

OA shows 21cm emission at velocities near -180 km s^{-1} (see Figure 1 in Tripp et al. 2003), but mostly the OA is not detected at this velocity in 21 cm emission. However, the HVC Complex C, which is close to the OA as shown in Figure 1, has a pervasive and highly extended “high-velocity ridge” at $v \approx -180 \text{ km s}^{-1}$ (Tripp et al. 2003). This high-velocity ridge has a similar morphology to the lower-velocity part of Complex C and is almost certainly a component of Complex C. The discovery by Lehner & Howk that the Outer Arm has a similar higher-velocity component at $v \approx -180 \text{ km s}^{-1}$ suggests that the OA and Complex C could be closely related. That the higher-velocity part of the OA is not apparent in most of the 21cm emission map likely indicates that the HI column density in the $v_{\text{LSR}} = -180 \text{ km s}^{-1}$ component is too low to be detected in 21cm emission. The $v_{\text{LSR}} = -180 \text{ km s}^{-1}$ component is significantly weaker in the UV absorption lines than the $v_{\text{LSR}} = -118 \text{ km s}^{-1}$ component (see Figure 1 in Lehner & Howk 2010), which is consistent with its absence in the 21cm emission map. All together, these observations suggest that Complex C and the OA (and possibly some of the other nearby HVCs) could have a common origin, and the gas becomes more highly ionized and ablated approaching the plane, an idea which is supported by the O VI/H I ratios in Complex C (Tripp et al. 2003; Sembach et al. 2003) as well as its morphology in high-resolution maps (Hsu et al. 2011). However, other explanations remain viable. For example, the HVCs with higher absolute velocities tend to be more highly ionized, and it is possible that as the HVCs approach the disk, they are decelerated and compressed, and the increased density from compression moves the gas into a less ionized state.

The highly anomalous velocity observed by Lehner & Howk indicates that the OA is truly a high-velocity cloud. If the OA is an outer spiral arm or part of the Galactic warp, then a mechanism to produce the high-

² The Galactocentric radius originally reported in Lehner & Howk (2010) was miscalculated (N. Lehner, private communication), and the correct R_G is listed here.

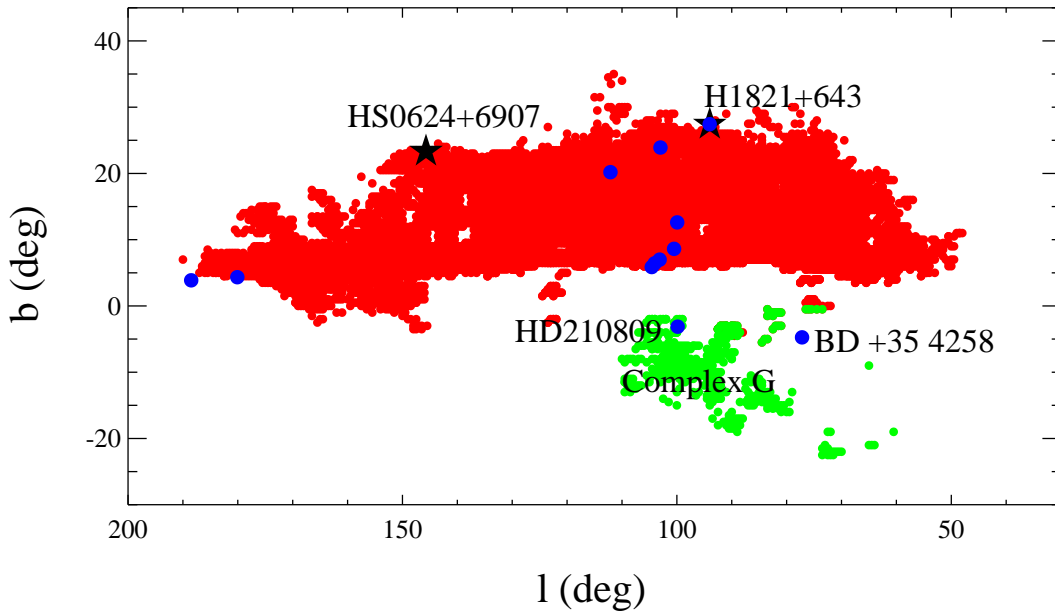


FIG. 2.— Map of the 21cm emission from the Outer Arm (red dots) and Complex G (green dots) from the Leiden-Argentine-Bonn Survey (Kalberla & Haud 2006). The locations of stars that we have used to search for absorption at Outer Arm velocities (see Table 4) are marked with blue circles, and the sight lines to the QSOs H1821+643 and HS0624+6907 are plotted with black stars. Note that the sight line to the central star of the planetary nebula K1-16 is very close to the H1821+643 sight line and falls nearly on top of the H1821+643 point. Toward BD +35 4258 and HD210809, highly significant UV absorption lines are detected at the velocity of Complex G (see Figures 11–12).

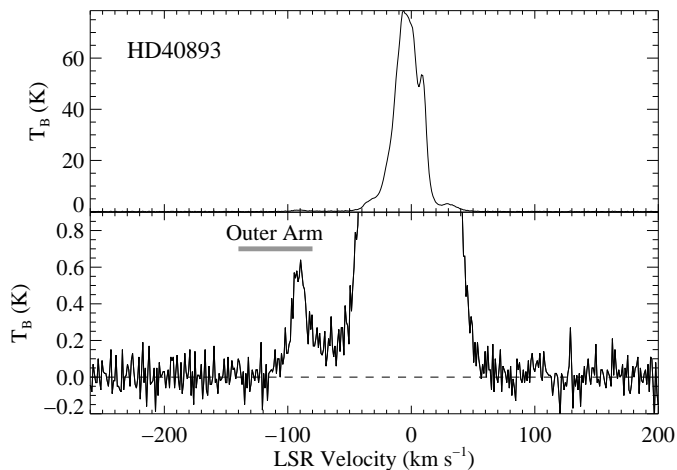


FIG. 3.— H I 21 cm emission in the direction of HD40893 from the Leiden/Argentine/Bonn (LAB) survey (Kalberla et al. 2005). Both panels plot brightness temperature vs. LSR velocity. In the lower panel, the gray bar shows the velocity range over which the Outer Arm is detected in absorption toward HS0624+6907.

velocity (-180 km s^{-1}) component must be identified. Moreover, the striking similarity of the Outer Arm and Complex C, both at the “main” HVC velocity and in the high-velocity ridge, must be explained. If Complex C and the Outer Arm are really related, then the OA might not be a spiral arm, and it is worthwhile to investigate other possible origins for this large H I cloud. We note that in this case, the “Outer Arm” shown in Figure 1 may be a different entity, at least in part, than the Outer Arm on the far side of the galaxy (e.g., Strasser et al. 2007; Dame & Thaddeus 2011), which is observed at lower latitudes and lower velocities.

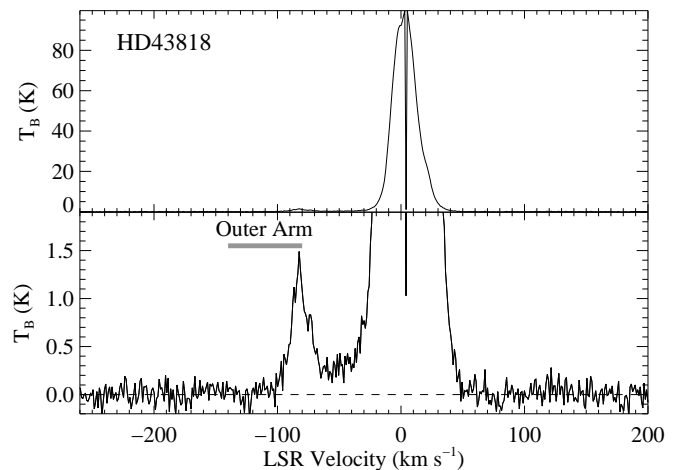


FIG. 4.— H I 21 cm emission in the direction of HD43818 from the LAB Survey, as in Figure 3.

Ultraviolet absorption lines provide a powerful means to learn about the nature of the Outer Arm. To probe the nature of the OA using UV absorption spectroscopy, we present below a study of two bright low-redshift QSOs, H1821+643 ($l = 94.00^\circ, b = 27.42^\circ, z_{\text{QSO}} = 0.297$) and HS0624+6907 ($l = 145.71^\circ, b = 23.35^\circ, z_{\text{QSO}} = 0.370$), lying in Galactic directions that pierce the Outer Arm (Figure 1). The sight line to the bright, low-redshift quasar H1821+643 ($z = 0.297, V = 14.24$) has been often used in studies of the galactic and intergalactic medium (e.g., Savage et al. 1995, 1998; Tripp et al. 2000, 2001; Oegerle et al. 2000; Narayanan et al. 2010), and consequently there are high-quality, high-resolution UV spectra of this target available from the *HST* and *FUSE*

archives. HS0624+6907 was included in the survey of Tripp et al. (2008), and thus high-quality UV spectra are also available for this sight line.

A number of stars in the general direction of the Outer Arm (and its adjacent HVCs) have also been observed with high resolution and high S/N with the Space Telescope Imaging Spectrograph (STIS) on *HST*. We will examine the STIS spectra of these stars to bolster the OA distance constraints from Lehner & Howk (2010). For reference, we overplot the locations of the targets on the 21 cm emission map of the Outer Arm from the Leiden/Argentine/Bonn (LAB) survey (Kalberla et al. 2005; Kalberla & Haud 2006) in Figure 2. We will show below that the HVC Complex G, which has similar kinematics to Complexes C and H and the Outer Arm (see Figure 1), is at a similar distance as the OA and Complex C. To aid this discussion, we also show the location of Complex G in Figure 2 along with the locations of two stars that constrain its distance. From Figure 2, it is difficult to judge if the two stellar sight lines (HD40893 and HD43818) at the high-longitude tip of the OA are truly in the direction of this cloud. However, as shown in Figures 3 and 4, the LAB spectra in the directions of these stars clearly show 21 cm emission at the OA velocity, and we will show below that UV absorption is detected at OA velocities in the spectrum of HD 43818 (§5). We note that HD43818 is in a direction where Milky Way gas is known to exhibit kinematic complexity (e.g., Burton & Moore 1979) including the “anticenter shell” (e.g., Heiles 1984). It has been argued that this structure is not a coherent shell (e.g., Tamanaha 1997), and we agree: the positive-latitude portion of the anticenter shell connects contiguously in space and velocity with the Outer Arm, and the negative-latitude part is a component of a large and distinct complex of HVCs with a much larger angular extent than the original anticenter shell (see Figure 1).

3. OBSERVATIONS

All of our targets, both stellar and quasistellar, have been observed with the E140M or E140H echelle modes of STIS. The QSOs have also been observed with *FUSE*. Information about the observations of H1821+643 and HS0624+6907, and about the reduction of the data, can be found in Tripp et al. (2001,2008) and Aracil et al. (2006). Table 1 provides a log of the STIS observations of stars that we use to constrain the distance to the OA and HVC Complex G in §5. The STIS spectra of these stars have also been reduced as described in Tripp et al. (2001). Information on the design and performance of STIS can be found in Woodgate et al. (1998) and Kimble et al. (1998); the design and performance of *FUSE* has been discussed by Moos et al. (2000,2002) and Sahnou et al. (2000).

The STIS observations of H1821+643 and HS0624+6907 were obtained with the E140M echelle mode with the $0.''2 \times 0.''06$ slit; this mode provides 7 km s^{-1} resolution (FWHM) and covers the 1150 – 1730 Å range. The *FUSE* data for these sight lines were obtained with the large ($30'' \times 30''$) aperture in all four *FUSE* channels (see Moos et al. 2000), which provide a resolution of $\approx 20 \text{ km s}^{-1}$ and cover the 905 – 1187 Å range. However, the S/N is very low in the *FUSE* SiC spectra of HS0624+6907, which cover $\lambda \lesssim 1000 \text{ Å}$, so

for that sight line we only use *FUSE* data from the LiF channels. To maximize the S/N of the HS0624+6907 spectra, we combine the *FUSE* spectra recorded during both the day and night sides of the *FUSE* orbit. This leads to inclusion of strong emission lines from the Earth’s atmosphere that are excited by sunlight and thus are predominantly present on the day side of the orbit. Fortunately, most of the Outer Arm absorption lines of interest are at a velocity that shifts the lines well away from the terrestrial dayglow emissions. For H1821+643, the *FUSE* data have substantially higher S/N, so we use the data from all four *FUSE* channels but only include the orbital-night photons in order to suppress the strong dayglow emission lines. Figure 5 shows the final coadded and continuum-normalized data for Galactic absorption lines of interest toward H1821+643, and Figure 6 shows Galactic absorption lines in the spectrum of HS0624+6907.

The measurements of H I 21 cm emission along the two QSO sight lines were obtained by Wakker et al. (2001) using the Effelsberg 100m telescope, which has a $9'$ beam. Both of the spectra show multiple well-defined velocity components, and we focus on the high-velocity 21 cm components which are associated with the Outer Arm. According to Wakker et al. (2001), the detected Outer Arm component in the direction of H1821+643 has $v_{\text{LSR}} = -128 \text{ km s}^{-1}$ and $N(\text{H I}) = (3.3 \pm 0.5) \times 10^{18} \text{ cm}^{-2}$, and toward HS0624+6907, the Outer Arm is detected at $v_{\text{LSR}} = -100 \text{ km s}^{-1}$ with $N(\text{H I}) = (19.8 \pm 1.8) \times 10^{18} \text{ cm}^{-2}$. However, Wakker et al. (2001) have compared their Effelsberg data to H I measurements of the same targets with smaller beams ($1' - 2'$, see their Table 1), and they conclude that the larger Effelsberg beam introduces systematic uncertainties at the level of $\approx 25\%$. For this reason, we include an additional 25% uncertainty in these H I column densities.

4. ABSORPTION-LINE MEASUREMENTS

We use two techniques to extract information from the ultraviolet absorption lines presented in this paper. First, we construct apparent column density profiles using the apparent optical depth (AOD) method (Savage & Sembach 1991). In brief, in this method the optical depth of absorption in a pixel at velocity v is first determined from the usual relation, $\tau_a(v) = \ln[I_c(v)/I_{\text{ob}}(v)]$, where $I_{\text{ob}}(v)$ is the observed flux and $I_c(v)$ is the continuum flux. We estimate the continuum flux [and normalize $I_{\text{ob}}(v)$] by fitting a low-order polynomial to the adjacent continuum near an absorption line of interest; typically we use the region within roughly $\pm 1000 \text{ km s}^{-1}$ of the line for continuum fitting. The apparent column density at v is then determined from the apparent optical depth, $N_a(v) = (m_e c / \pi e^2) (f \lambda)^{-1} \tau_a(v) = 3.768 \times 10^{14} (f \lambda)^{-1} \tau_a(v)$, where f is the oscillator strength and λ is the transition wavelength in Å. The other symbols have their common meanings. One virtue of this approach is that the effects of line saturation can be quickly and easily recognized by comparing the $N_a(v)$ profiles of two or more resonance lines of a given species which differ in the product $f \lambda$. Detailed discussions of the use and benefits of the AOD technique can be found in Savage & Sembach (1991) and Jenkins (1996).

We will find the $N_a(v)$ method to be illustrative, but as we can see from Figures 5 - 6, many of the Outer Arm ab-

TABLE 1
LOG OF STIS ECHELLE OBSERVATIONS OF STARS IN THE DIRECTION OF
THE OUTER ARM

Star	Observation Date	Integration Time (seconds)	STIS Grating ^a	MAST ID ^b
HD40893 ...	2004 Feb. 20	10064	E140H	O8NA02010,20
HD43818 ...	2001 Apr. 9	1440	E140M	O5C07I010
HD198781 ..	1999 Sept. 5	360	E140H	O5C049010
HD201908 ..	1999 Sept. 21	360	E140H	O5C051010
HD203374 ..	2002 Dec. 24	600	E140M	O6LZ90010
HD207198 ..	2000 Oct. 30	4711	E140H	O59S06010,20
HD208440 ..	1999 Nov. 5	720	E140H	O5C06M010
HD209339 ..	2002 Aug. 7	1200	E140H	O6LZ92010
	2006 Dec. 28	1416	E140H	O5LH0B010,20
HD210809 ..	1999 Oct. 30	720	E140H	O5C01V010
BD+35 4258	2003 Mar. 15	1200	E140M	O6LZ89010

^a All of the observations used the $0.2'' \times 0.2''$ STIS aperture except the observation of HD207198, which was recorded with the $0.2'' \times 0.09''$ slit, and the longer-wavelength observation of HD209339 (obtained 2006 Dec. 28), which used the $0.1'' \times 0.03''$ aperture.

^b Identification code for the data in the Multimission Archive at Space Telescope (see <http://archive.stsci.edu/index.html>).

TABLE 2
OUTER-ARM PROFILE-FITTING MEASUREMENTS: H1821+643

Species	Fitted Lines (Å)	v (LSR) (km s ⁻¹)	b (km s ⁻¹)	log [N (cm ⁻²)]
O I	971.73, 976.45, 1302.17	-145 ± 1 -131 ± 1 -111 ± 1	4 ± 1 7 ± 2 9 ± 3	14.43±0.15 14.64±0.11 14.06±0.09
N I	1199.55 ^a	-146 ± 2: -133 ± 1:	6 ⁺⁴ ₋₃ : 2 ⁺⁴ ₋₁ :	13.19±0.13 13.14±0.19
S II	1253.81,1259.52 ^b	-131 ± 2:	15 ± 1:	14.02±0.08:
Al II	1670.79	-148 ± 2 -132 ± 4 -113 ± 8	4 ⁺⁸ ₋₃ 12 ⁺⁸ ₋₅ 11 ⁺⁹ ₋₅	12.12±0.35 12.82±0.26 12.45±0.58
Si II	1190.42, 1193.29, 1260.42, 1304.37, 1526.71	-147 ± 1 -134 ± 1 -117 ± 4	5 ± 1 9 ± 3 11 ± 4	13.27±0.20 13.88±0.16 13.71±0.19
Fe II	1121.98, 1125.45, 1142.37 1143.23, 1144.94, 1608.45	-145 ± 1 -134 ± 1 -128 ± 9	4 ⁺¹¹ ₋₃ 3 ⁺⁴ ₋₂ 15 ⁺⁹ ₋₆	13.15±0.55 13.25±0.31 13.64±0.31
C IV	1548.20,1550.78	-213 ± 1 -151 ± 3 -131 ± 4	9 ± 1 5 ⁺¹⁰ ₋₃ 14 ⁺⁸ ₋₅	13.25±0.03 12.59±0.37 13.28±0.40
Si IV	1393.76,1402.78 ^c	-111 ± 14 -150 ± 1 -125 ± 2 -99 ± 9	33 ± 11 4 ± 1 16 ± 3 10 ⁺¹⁹ ₋₇	13.80±0.09 12.40±0.11 13.17±0.07 12.45±0.35

^a For N I, only a single, relatively weak transition is free of blending in the STIS spectrum, and consequently the N I measurements should be treated with caution (at Outer Arm velocities, the N I $\lambda\lambda$ 1200.22, 1200.71 transitions are blended with lower-velocity absorption in the other lines of the N I triplet). In addition, the third component that is evident in the other metal profiles (at $v \approx -117$ km s⁻¹) is too weak to be fitted in the N I λ 1199.55 profile.

^b The S II λ 1259.52 profile is corrected for blending with an extragalactic O VI absorber (see text). The S II measurements should also be treated with caution because they are weak and marginally detected. Only a single component could be fitted to these weak lines.

^c As can be seen from Figure 8, there is a discrepancy between the Si IV λ 1393.76 and λ 1402.78 profiles at $-115 \lesssim v_{\text{LSR}} \lesssim -80$ km s⁻¹. This discrepancy is due to an H I Ly α line at $z_{\text{abs}} = 0.14760$ that blends with the Galactic Si IV λ 1393.76 profile. The identification of this blend as this H I Ly α line is established by the presence of an H I Ly β line at this z in the *FUSE* spectrum of H1821+643 (K. R. Sembach et al., in preparation).

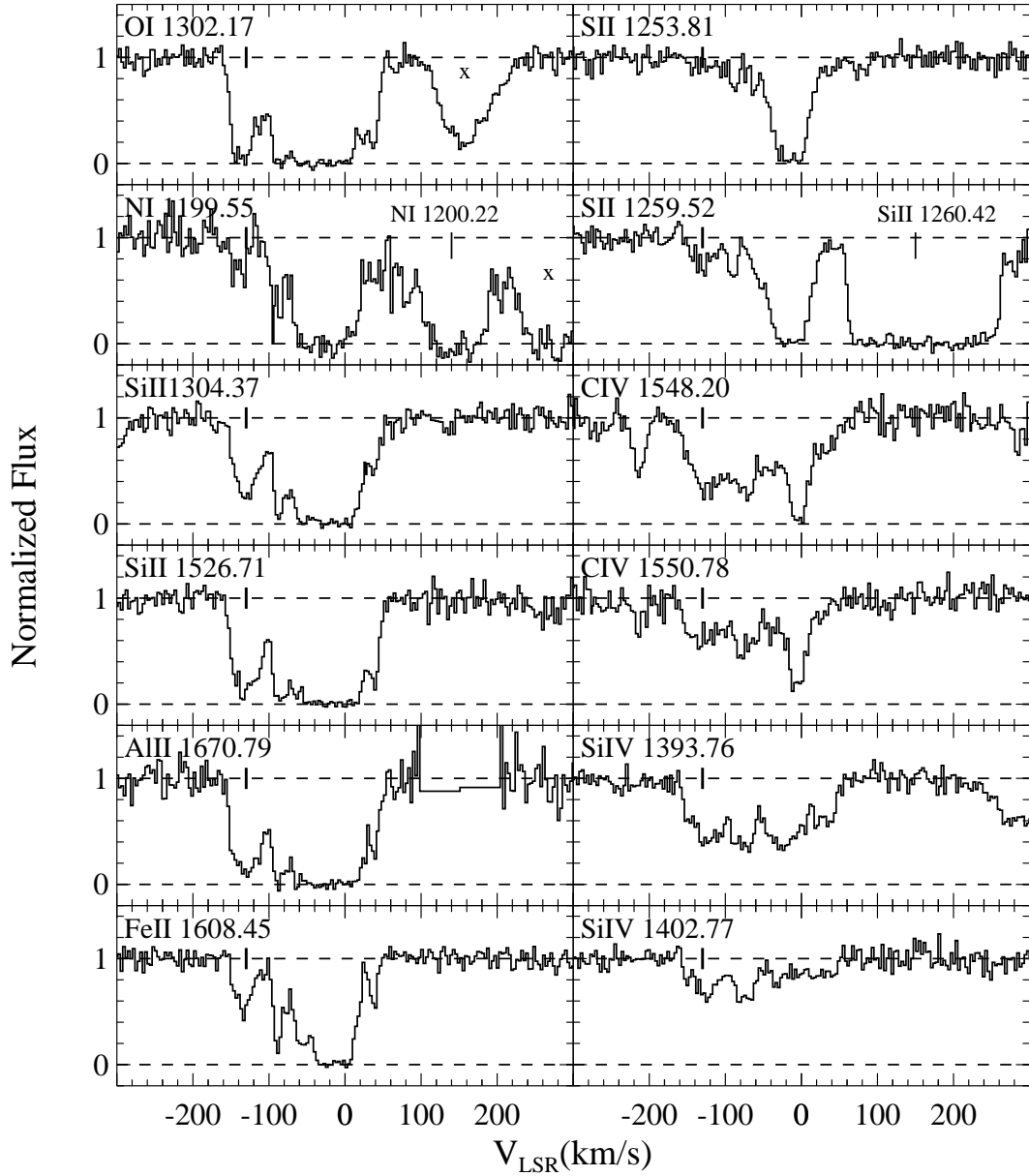


FIG. 5.— Continuum-normalized UV absorption profiles of Galactic lines detected in the STIS E140M echelle spectrum of H1821+643, plotted vs. LSR velocity. The profile transition is indicated in each panel. In some panels, other Milky Way lines that happen to fall within the plotted velocity range are labeled; some other unrelated absorption features are marked with an 'x'. The Al II λ 1670.79 line is near a gap between the STIS echelle orders, and there is no data between $v = 100$ and 200 km s $^{-1}$. The Outer Arm components, at $v_{\text{LSR}} \approx -130$ km s $^{-1}$, are marked with a vertical tick mark.

TABLE 3
OUTER-ARM PROFILE-FITTING MEASUREMENTS: HS0624+6907

Species	Fitted Lines (Å)	v (LSR) (km s ⁻¹)	b (km s ⁻¹)	$\log [N \text{ (cm}^{-2}\text{)}]$
N I.....	1199.55,1200.22 ^a	-104 :	5 :	$\gtrsim 14.6 :$
Si II.....	1190.42,1193.29,1260.42 1304.37,1526.71 ^a	-101 :	11 :	$\gtrsim 14.4 :$
S II.....	1253.81,1259.52	-100 ± 1	7 ± 1	14.18 ± 0.07
Al II.....	1670.79 ^a	-104 :	10 :	$\gtrsim 13.00 :$
Fe II.....	1121.98,1143.23,1144.94 1608.45	-104 ± 1	8 ± 1	14.03 ± 0.06
C IV.....	1548.20,1550.78	-107 ± 1	5 ± 1	13.07 ± 0.11
Si IV.....	1393.76,1402.77	-101 ± 1	16 ± 1	13.06 ± 0.03

^a Due to line saturation, these measurements are highly uncertain.

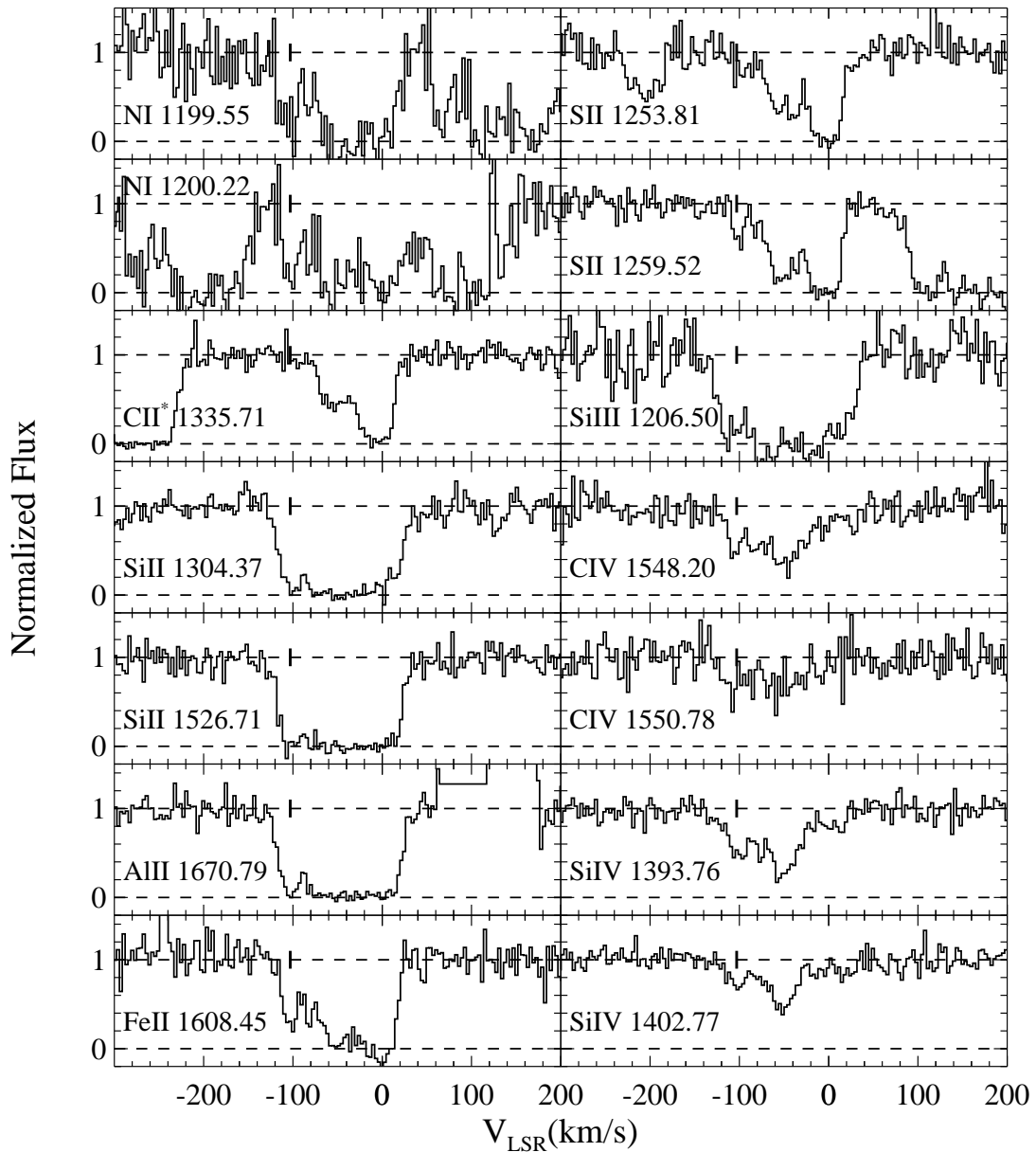


FIG. 6.— UV absorption lines detected in the STIS E140M echelle spectrum of HS0624+6907, as in Figure 5. The high velocity components affiliated with the Outer Arm are indicated with vertical tick marks, at $v_{\text{LSR}} \approx -100 \text{ km s}^{-1}$.

sorption lines of interest are blended with adjacent components at lower velocities, so we need to be able to deblend these features. Moreover, we will show evidence below that even the OA absorption itself is composed of closely spaced narrow components. Consequently, we use the Voigt-profile fitting software of Fitzpatrick & Spitzer (1997), including the effects of the STIS line-spread function (Proffitt et al. 2010), to measure the velocity centroids, column densities, and line widths (expressed as b -values) of the lines.

4.1. H1821+643

The Outer Arm absorption toward H1821+643 has been studied previously by Savage et al. (1995) and Tripp et al. (2003). However, the initial investigations assumed a single component for the OA absorption profile and only employed a subset of the currently available lines detected in the OA, so it is worthwhile to revisit these data.

Careful examination of the STIS H1821+643 data reveals that the OA component structure is more complicated than a single component. To show this, we compare the apparent column density profiles of selected species in Figure 7, and we plot expanded absorption profiles in Figure 8. Several features in these figures provide evidence of multiple components in the OA velocity range. First, the $N_a(v)$ profiles consistently show a sharp edge at $v_{\text{LSR}} = -150 \text{ km s}^{-1}$ in several different species. For example, both of the Si II profiles in panel (a) of Figure 7 show a consistent edge at this v , and the Fe II and Al II profiles (panel c) exhibit the same feature. Such a sharp discontinuity cannot occur in a profile due to a single Voigt component. Instead, this feature requires at least one narrow component near $v_{\text{LSR}} \approx -150 \text{ km s}^{-1}$ that is blended with another component at $v_{\text{LSR}} > -150 \text{ km s}^{-1}$. In fact, we can see from the Fe II $\lambda 1608.45$ and Si II $\lambda 1526.71$ lines (panel b) that there are indications of three components in the OA: a narrow feature at $v_{\text{LSR}} \approx -135 \text{ km s}^{-1}$ and a broader component at $v_{\text{LSR}} \approx -125 \text{ km s}^{-1}$ (in addition to the component causing the sharp edge at $v_{\text{LSR}} \approx -150 \text{ km s}^{-1}$). To show this a different way, we compare in Figure 8 a single-component fit to a three-component fit of the OA absorption profiles of Fe II $\lambda 1608.45$ and Al II $\lambda 1670.79$. The three-component fit is superior, both for fitting the sharp edge at $v_{\text{LSR}} \approx -150 \text{ km s}^{-1}$ and for fitting the detailed component structure at $v_{\text{LSR}} > -150 \text{ km s}^{-1}$. The χ^2 statistics for the fits indicate that the one-component fits are acceptable but the three-component fits are better. For example, for the Fe II $\lambda 1608.45$ line, the reduced χ^2 for the single-component fit is $\chi^2_\nu = 1.08$ while the three-component fit has $\chi^2_\nu = 0.93$. We note that we have also explored whether two-component fits might be favored. We find that the two-component fits provide no improvement compared to one-component fits; in this case, the profile-fitting code converges to a solution that is virtually identical with the one-component model with the same χ^2_ν . Three components are required to improve the fit to the sharp edge and the narrow core of the profiles.

Based on the consistent evidence in multiple profiles, we have elected to revise the profile fits published previously, and our results from fitting three components to the absorption lines detected in the OA are summarized

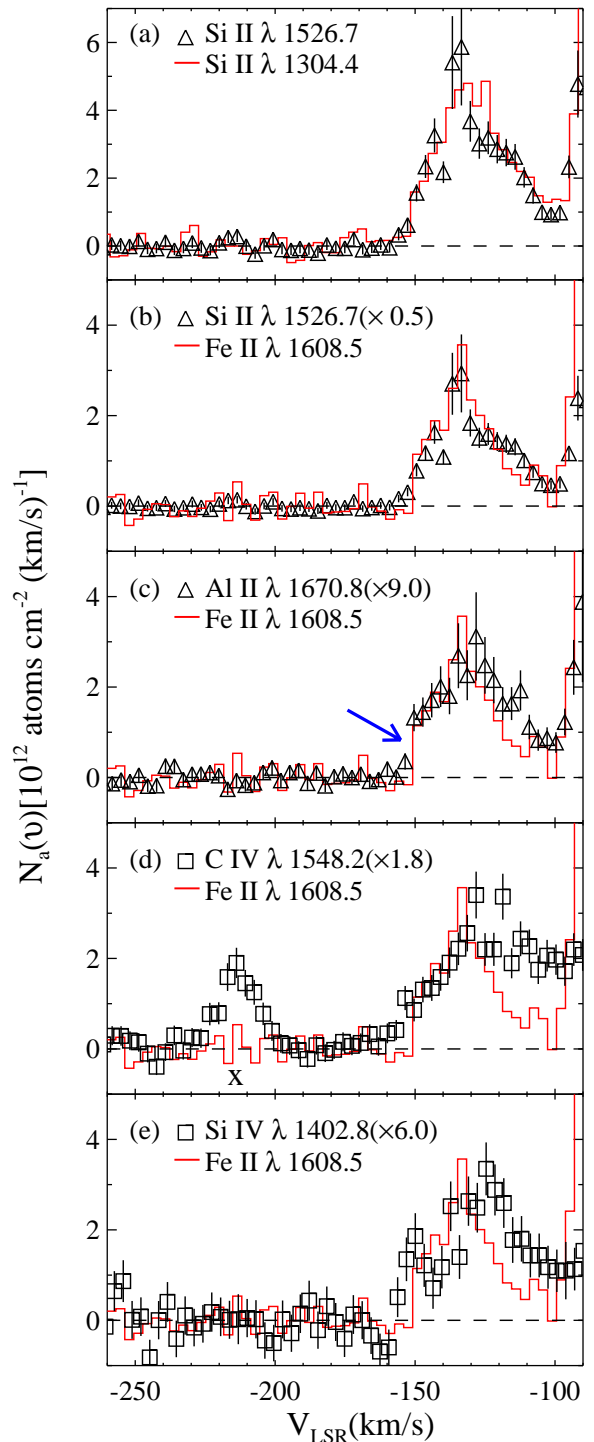


FIG. 7.— Comparison of various apparent column density profiles (§4) observed toward H1821+643 in the Outer Arm, plotted vs. LSR velocity. The panels show (a) Si II $\lambda 1304.4$ (red histogram) vs. Si II $\lambda 1526.7$ (triangles with 1σ error bars), (b) Fe II $\lambda 1608.5$ (red histogram) vs. Si II $\lambda 1526.7$ ($\times 0.5$, triangles), (c) Fe II $\lambda 1608.5$ (red histogram) vs. Al II $\lambda 1670.8$ ($\times 9.0$, triangles), (d) Fe II $\lambda 1608.5$ (red histogram) vs. C IV $\lambda 1548.2$ ($\times 1.8$, squares), and (e) Fe II $\lambda 1608.5$ (red histogram) vs. Si IV $\lambda 1402.8$ ($\times 6.0$, squares). A sharp edge is consistently present on the blue side of many of the profiles (indicated with a blue arrow in the Fe II vs. Al II comparison). The feature at $v_{\text{LSR}} = -213 \text{ km s}^{-1}$ is due to C IV and is confirmed by the other line of the C IV doublet, but no other metals are detected at that velocity, with the possible exception of O VI (see Tripp et al. 2003).

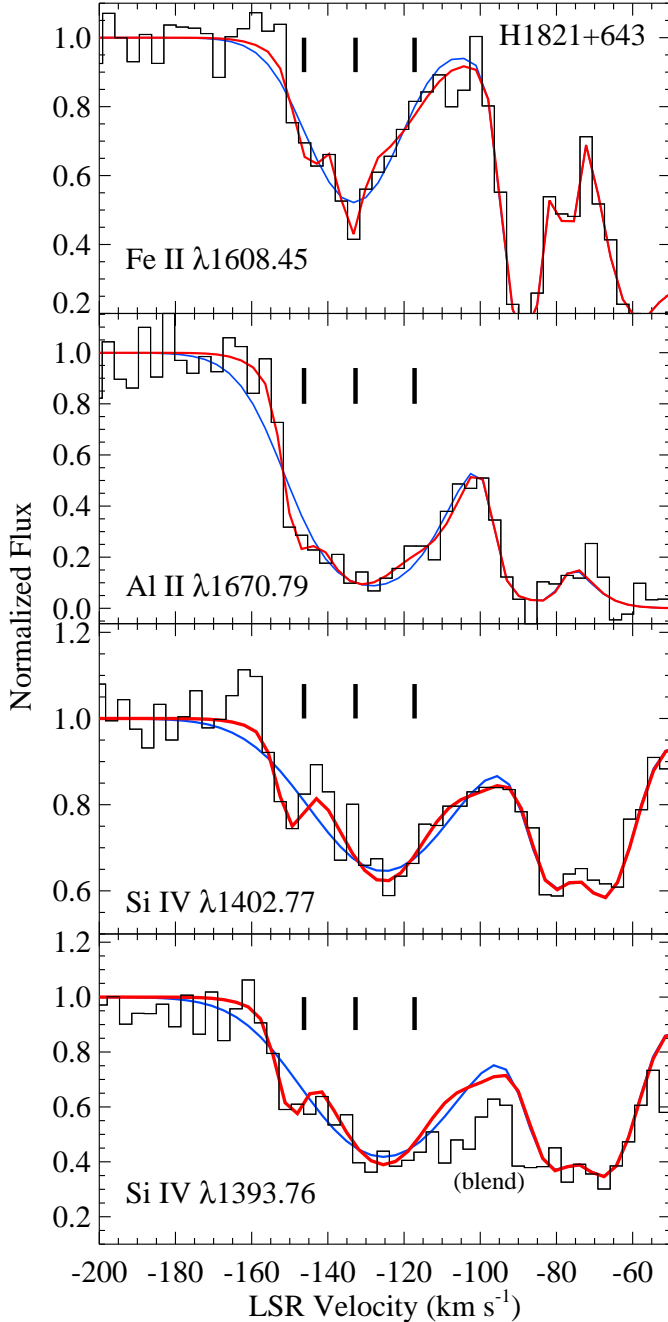


FIG. 8.— Comparison of a Voigt-profile fit to the H1821+643 Outer Arm component (at $v \approx -130 \text{ km s}^{-1}$) assuming a single component for the OA (smooth blue line) or 3 components for the OA (smooth red line). The fits are overlaid on the observed profiles (histograms) of Fe II $\lambda 1608.45$, Al II $\lambda 1670.79$, and Si IV $\lambda \lambda 1393.76, 1402.77$, as labeled in each panel. For components at velocities outside of the OA velocity range, the two models have identical component structure. Comparison of the one-component and three-component fits show that the three-component fit provides a better fit to the detailed sharp features that consistently appear in various profiles (as also shown in Figure 7).

in Table 2. Interestingly, many of the line widths indicated by the fits are relatively narrow, which potentially has implications regarding the physical conditions of the gas (§6). We note that it can be difficult to extract reliable line widths from strongly blended components, but the presence of the sharp edge in many of the absorption profiles requires a narrow component in many of the species. This alone has interesting implications about the nature of the OA. We note that most of the OA metals in Table 2 are not saturated, and the column densities summed over the three components or determined from a single component are quite similar and are robust.

Perhaps even more interesting is the indication of a similarly narrow component in the profiles of the highly ionized species Si IV and C IV (see Figure 5). A narrow feature can be seen consistently in the Si IV $\lambda \lambda 1393.76, 1402.77$ doublet at $v_{\text{LSR}} = -150 \text{ km s}^{-1}$; to show this we again plot the Si IV doublet, with single-component and a three-component fits overlaid, in the lowest panels in Figure 8. In the high ions, this narrow feature is offset to somewhat more negative velocities than in the low ions, but it is clearly present. This is interesting because in collisionally ionized gas, species ionized to this degree should be much broader due to the higher temperature of the plasma. We will return to this issue in §6.

We note that in the spectrum of H1821+643, the measurement of S II in the Outer Arm is somewhat complicated by blending with an extragalactic O VI doublet at $z_{\text{abs}} = 0.21331$ (Tripp et al. 2008); the O VI $\lambda 1037.62$ line at this z is blended with the S II 1259.52 transition at the Outer Arm velocity. The presence of the O VI $\lambda 1037.62$ in the blend is indicated by a comparison of the S II $\lambda 1253.83$ and $\lambda 1259.52$ $N_a(v)$ profiles: the 1259.52 \AA line indicates a greater apparent column than the 1253.83 \AA transition, which is unphysical (the lines should indicate the same column or, if there is some saturation, the $\lambda 1253.83$ line should be greater than $\lambda 1259.52$). This discrepancy is caused by extra optical depth in the $\lambda 1259.52$ profile contributed by the extragalactic O VI line. To overcome this problem, we used the O VI $\lambda 1031.93$ line at $z_{\text{abs}} = 0.21331$, which is free from blending, to predict the profile of the corresponding O VI $\lambda 1037.62$ line, and then we divided the predicted O VI $\lambda 1037.62$ profile out of the O VI + S II blend. After removing the extragalactic O VI, we found the $N_a(v)$ profiles of S II $\lambda 1253.83$ and $\lambda 1259.52$ to be in good agreement.

4.2. HS0624+6907

Toward HS0624+6907, the ultraviolet absorption in the Outer Arm concentrates near $v_{\text{LSR}} = -100 \text{ km s}^{-1}$ (see Figure 6), in agreement with the 21 cm emission velocity reported by Wakker et al. (2001). The measurements of the OA absorption lines in the spectrum of this QSO are summarized in Table 3. Unfortunately, because the gas column density is substantially higher toward HS0624+6907, many of the species that imprint absorption on the HS0624+6907 spectrum at OA velocities are difficult to measure due to line saturation. The *FUSE* SiC data do not have adequate S/N, so the only transitions available for O I are strongly saturated and do not yield useful measurements. The N I triplet at $\approx 1200 \text{ \AA}$ is weaker, but comparison of the N I $\lambda 1199.55$ and $\lambda 1200.22$ $N_a(v)$ profiles indicates that these lines are also affected by saturation, even in the weakest compo-

TABLE 4
HELIOCENTRIC AND GALACTOCENTRIC DISTANCES OF STARS IN THE DIRECTION OF THE OUTER ARM AND ADJACENT HVCs

Star	Galactic Coordinates		Distance ^a (kpc)	Galactocentric Radius ^b (kpc)	z (kpc)	Reference ^c	log $N(\text{C II})$	log $N(\text{Si II})$
	Long.	Lat.						
<u>Outer Arm Nondetections</u>								
K1-16	94.03	+27.43	1.6	8.7	0.7	1
HD198781 . . .	99.94	+12.61	0.69	8.6	0.2	2	<12.31 ^d	<12.58 ^d
HD203374 . . .	100.51	+8.62	0.34	8.6	0.1	3	≤12.88 ^e	<12.41 ^d
HD207198 . . .	103.14	+6.99	1.3	8.9	0.2	2	<12.23 ^d	<12.52 ^d
HD208440 . . .	104.03	+6.44	1.1	8.8	0.1	4	<12.42 ^d	<12.64 ^d
HD209339 . . .	104.58	+5.87	1.2	8.9	0.1	4	<12.40 ^d	<12.33 ^d
HD201908 . . .	112.40	+20.19	0.13	8.6	0.04	5	<12.34 ^d	<12.52 ^d
HD40893	180.09	+4.34	3.1	11.6	0.2	4	<12.35 ^d	<12.36 ^d
<u>Outer Arm Detections</u>								
HS1914+7139	102.99	+23.91	14.9	17.6	6.04	6,7	...	≈13.6
HD43818	188.49	+3.87	1.9	10.4	0.1	4	13.50±0.02	12.84±0.11
<u>Complex G Detections</u>								
BD+35 4258 . .	77.19	-4.74	2.9	8.4	-0.2	8	14.04±0.02	12.43±0.14
HD210809 . . .	99.85	-3.13	4.3	10.2	-0.2	2	13.70±0.01	11.82±0.03

^a Heliocentric distance to the star.

^b Galactocentric radius, $R_G^2 = R_0^2 + (r \cos b)^2 - 2rR_0 \cos l \cos b$, where (l, b) are the Galactic coordinates and r is the Heliocentric distance of the target, assuming the distance from the Sun to the Galactic center $R_0 = 8.5$ kpc.

^c Source of the Heliocentric stellar distance: (1) Oegerle et al. (2000), (2) Bowen et al. (2008), (3) Jenkins & Tripp (2001), (4) Jenkins & Tripp (2011), (5) Fitzpatrick & Massa (2005), (6) Lehner & Howk (2010), (7) Ramspeck et al. (2001), (8) Jenkins (2009). As discussed in Appendix B of Bowen et al. (2008), the uncertainties in the stellar distances range from 10% to 30%.

^d Upper limit derived from the 3σ equivalent width limit, assuming the line is on the linear part of the curve of growth.

^e A marginally significant feature is present in the Outer Arm velocity range toward HD203374. However, the feature is very broad and shallow and is highly sensitive to continuum placement – a slightly lower continuum placement would mostly remove the feature. In addition, the feature is not corroborated by other strong interstellar lines, e.g., the Si III profile shows no evidence of absorption in this velocity range. Given the lack of corroborating evidence and marginal significance of the line, we treat this feature as an upper limit.

ment at the OA velocity. Moreover, because the N I lines are quite noisy, it is difficult to accurately assess and correct for the saturation, so we conservatively treat the N I measurement as a lower limit. The available Si II transitions are also strong and saturated. Fortunately, the Outer Arm is detected in the S II $\lambda\lambda 1253.81, 1259.52$ transitions toward HS0624+6907 (see Figure 6), and the S II $N_a(v)$ profiles are in good agreement, so we can obtain a reliable measurement of the metallicity of the OA toward this QSO.³ Sulfur is advantageous because it is thought that it does not deplete strongly onto dust and thus provides a measurement of the overall (gas-phase) metallicity (Savage & Sembach 1996, but see the caveats noted by Jenkins 2009). The Fe II $\lambda 1608.45$ line should also be weak enough to yield a good column density, and in this case we can employ a set of weaker Fe II lines from the *FUSE* LiF spectra to ensure that the column is reliably measured. Since iron is highly prone to dust depletion, this provides insight on the presence of dust in the OA. The Al II $\lambda 1670.79$ line is the only Al II transition available and is strong enough to be confused by saturation, but in principle this line can still be used to corroborate the presence/absence of dust indicated by the Fe II measurement. As we can see from Figure 6, the Si IV and C IV doublets are clearly detected in the OA toward HS0624+6907. The Si IV $N_a(v)$ profiles are in excellent agreement, and thus the Si IV lines are not saturated. While the C IV $\lambda 1550.78$ transition is relatively noisy, the C IV $N_a(v)$ profiles also appear to be in satisfactory agreement and are unlikely to be badly saturated.

³ Absorption at the OA velocity is also apparent in the weakest S II transition at 1250.58 Å, but the line detection is quite marginal, so we only use the two stronger S II lines for the measurements.

5. DISTANCE OF THE OUTER ARM AND COMPLEX G

The kinematical similarity of the Outer Arm, Complex C, Complex G, and Complex H evident in Figure 1 is intriguing. Since Complex C has been shown to be relatively nearby (Wakker et al. 2007; Thom et al. 2008), and the OA is not that much farther (if it is farther at all), it is possible to test whether these clouds are related by constraining their distances. For this reason, we have searched the STIS archive for stellar spectra with implications regarding the distances of these HVCs.

5.1. The Outer Arm

As discussed above, the new constraint on the distance to the Outer Arm from Lehner & Howk (2010) raises a question about the nature of this gas cloud. However, this constraint is derived from a single sight line through a highly extended object (see Figures 1 - 2). As we commented above, the kinematic similarity and spatial proximity (projected on the sky) of the OA and Complex C (and other outer-galaxy HVCs) suggests a possible connection. Nevertheless, these objects could be at different radial distances and thus could still be unrelated. However, Complex C has been shown to be at a Heliocentric distance of ≈ 10.5 kpc (Wakker et al. 2007; Thom et al. 2008), or a Galactocentric radius of $\approx 12.3 - 13.7$ kpc for the three directions in which it has been detected toward stars. Therefore, the Outer Arm and Complex C have similar radial distances and their three-dimensional locations are also consistent with a common origin.

As shown in Figures 1 - 2, the OA has a large angular extent, so it is not difficult to find bright stars at a variety of distances in its direction. To more tightly constrain the location and nature of the OA, in this section we present a minisurvey for OA absorption toward stars. There are many high-quality ultraviolet spectra of stars

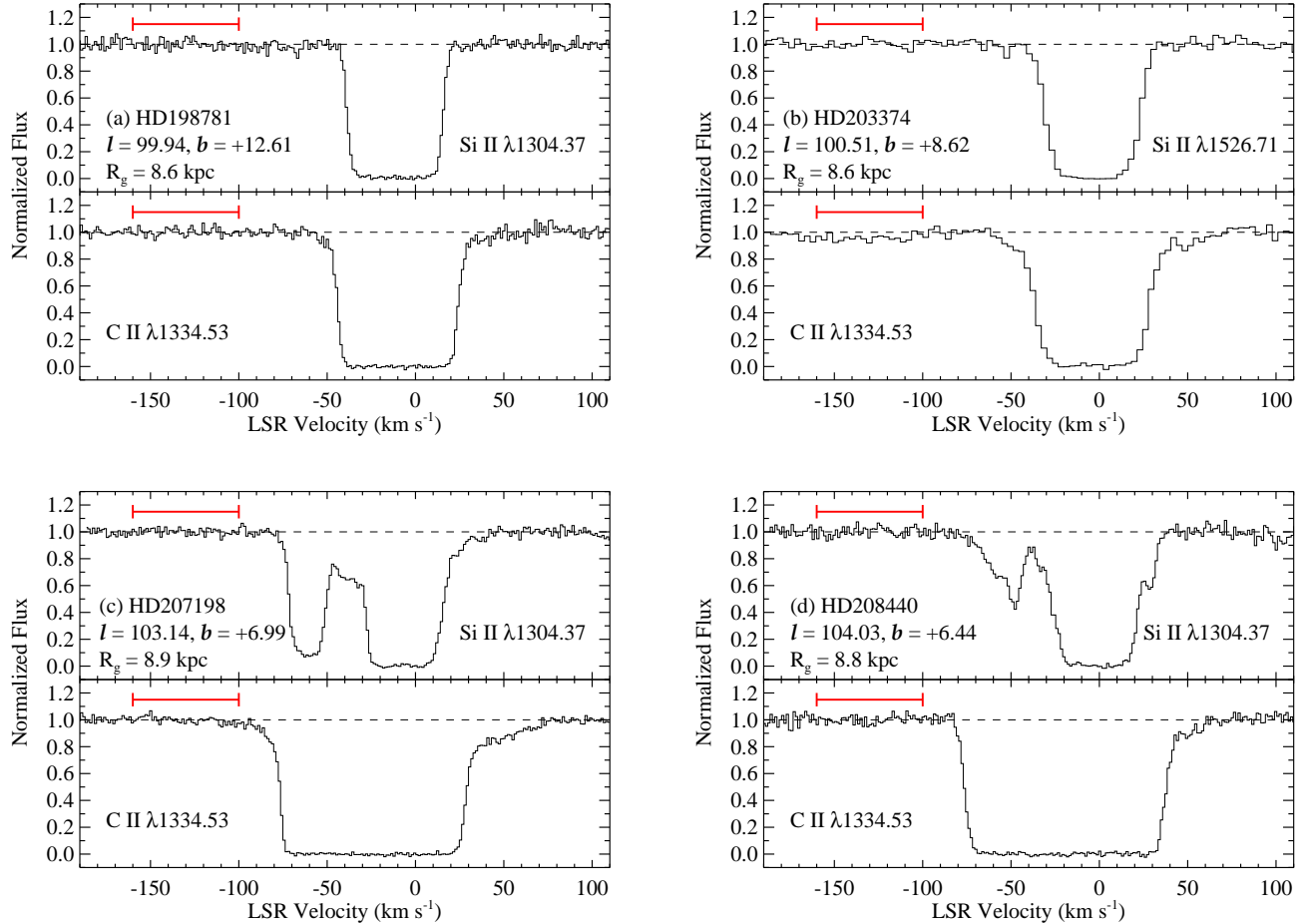


FIG. 9.— Continuum-normalized STIS absorption profiles of strong interstellar lines in the spectra of the stars in the direction of the Outer Arm from Table 4: (a) HD198781, (b) HD203374, (c) HD207198, (d) HD208440, (e) HD209339, (f) HD201908, (g) HD40893, and (h) 43818. For comparison, absorption profiles of the same species from the spectra of H1821+643 and HS0624+6907 are shown in (i) and (j), respectively. For each sight line, the upper panel shows one of the Si II absorption profiles and the lower panel shows the C II λ 1334.53 line. The horizontal red bar in each upper panel indicates the velocity range over which OA absorption is detected toward H1821+643, except in the panels of HD40893 and HD43818; these stars are closer to HS0624+6907, so in these panels (g and h) the red bar shows the velocity range of the OA toward HS0624+6907. Despite high S/N ratios, only one star, HD43818, shows UV absorption in the velocity range of the OA (see Figure 10). Several intermediate-velocity absorption components detected toward H1821+643 are also evident toward HD207198, HD208440, and HD209339; these are likely to be affiliated with the Perseus arm.

in its general direction in the *HST* archive. We have selected a set of stars from the *HST* archive that have been observed with one of the STIS echelle modes at high-S/N ratio. The stellar sight lines that we selected for this search are indicated on the map of the OA in Figure 2 and are listed in Table 4 with their Galactic coordinates, Heliocentric and Galactocentric distances, z heights, and the source of the distance information. The continuum-normalized absorption profiles of strong interstellar lines of C II and Si II from the spectra of these stars are plotted in Figure 9 along with one of the interstellar lines from the H1821+643 and HS0624+6907 spectra for comparison.

We show both the C II and Si II lines in Figure 9 because while the C II lines are advantageous because they are the strongest low-ionization metal lines and thus are the most sensitive probes of low-density clouds, they are also disadvantageous because they often saturate strongly and consequently completely hide the sight line component structure. This component structure can be recognized in the weaker Si II lines while still retaining good sensitivity to low-column clouds. Several exam-

ples of these advantages and disadvantages are apparent from comparisons of the C II and Si II profiles in Figure 9. Measurements of (and upper limits on) $N(\text{C II})$ and $N(\text{Si II})$ derived from the stellar data are listed in Table 4. As expected, the C II limits are more stringent; comparing the column-density measurements and limits in Table 4 with Galactic ISM measurements in various contexts (see, e.g., Tripp et al. 2002, their §4 and Appendix), we see that the C II limits are often well below the C II column densities typically detected in the disk of the Milky Way, and the Si II limits are less constraining.

Several interesting results are evident from the information in Figure 9 and Table 4:

First, the Outer Arm is clearly detected in absorption toward one star, HD43818. As shown in Figure 10, C II and Si III absorption is nicely detected and well-aligned with the OA 21cm emission in this direction. Two UV absorption components are evident near the OA velocity; the column densities, b -values, and centroids of these components, measured by Voigt-profile fitting as discussed above, are listed in Table 5. The velocities ($|v|$) of the UV absorption and 21cm emission are some-

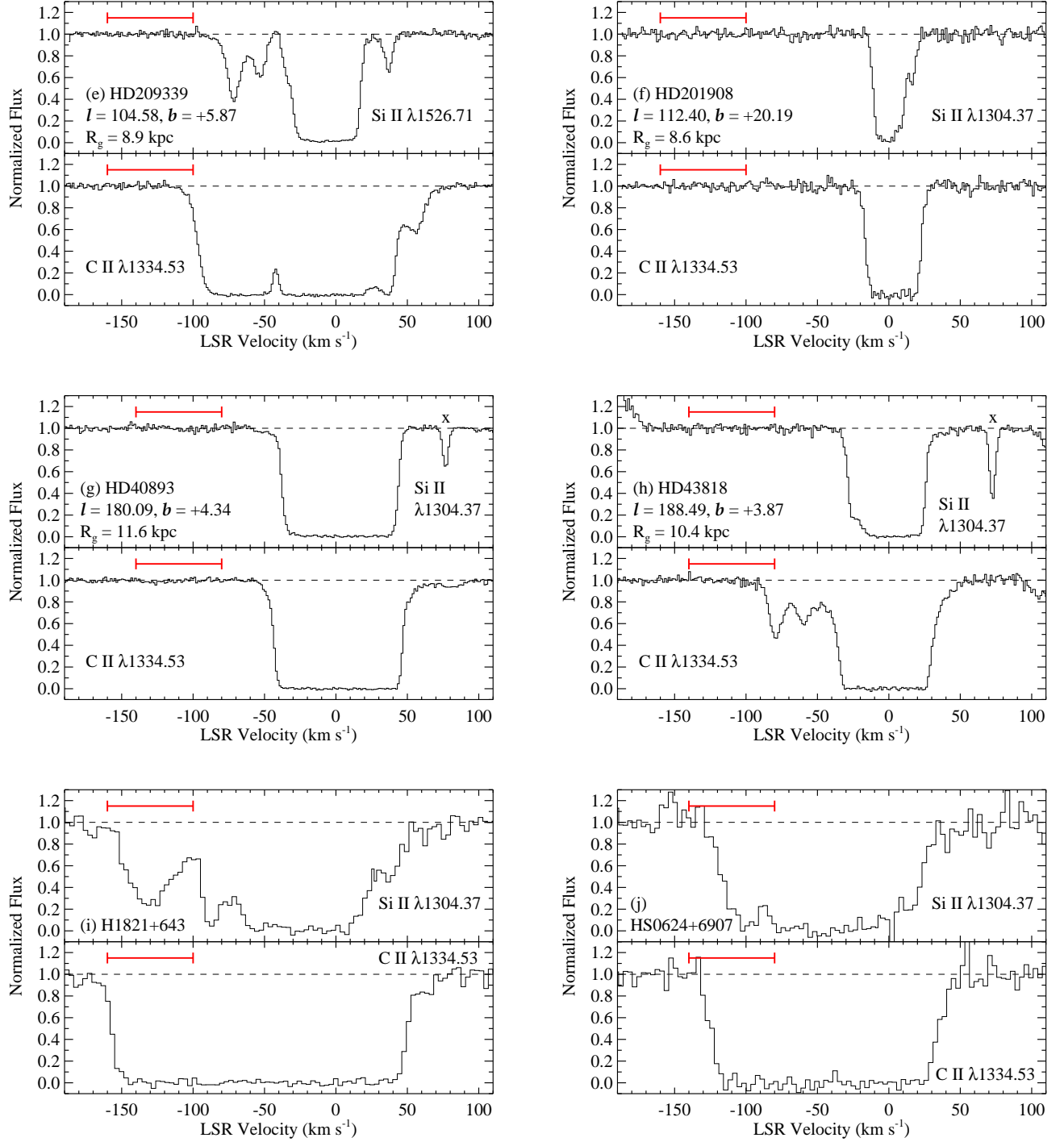


FIG. 9.— (continued)

what lower than the $|v|$ values in other parts of the OA, but the OA is known to have a velocity gradient with decreasing $|v|$ values in this region; the velocities are consistent with an origin in the Outer Arm. Of the nine stellar sight lines that we have examined toward the OA, the HD43818 sight line is the second-most distant target in both Heliocentric distance and Galactocentric radius (see Table 4), so it is perhaps not surprising that the OA is detected toward this target but not the others. This indicates that the OA is beyond the closer stars

but in front of HD43818, i.e., in the Galactocentric radius range of $9 < R_G \leq 10.4$ kpc. While the absence of UV absorption toward HD40893 would seem to be inconsistent with this result since HD40893 is at $R_G = 11.6$ kpc, we note that the 21 cm emission is substantially weaker toward HD40893 (compare Figures 3 and 4), and the lower column density toward HD40893 could cause the UV absorption to slip below the detection threshold. Moreover, the sight lines to HD40893 and HD43818 are relatively close on the sky, and the significant dif-

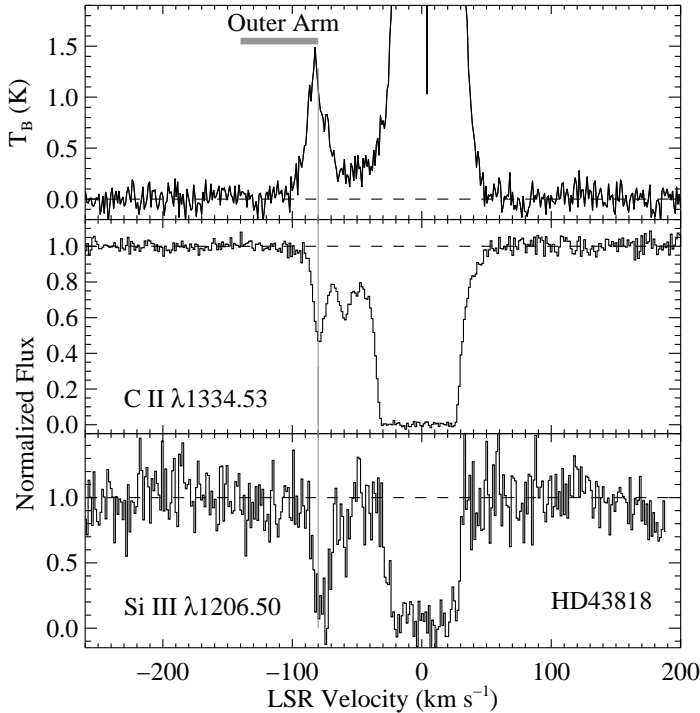


FIG. 10.— Comparison of the 21cm emission (from the LAB survey) in the direction of HD43818 (upper panel) to the ultraviolet absorption profiles of C II λ 1334.53 and Si III λ 1206.50 recorded with STIS (middle and lower panels, respectively). Significant C II and Si III absorption lines are clearly detected at the velocity of the OA 21 cm emission.

ferences in the LAB 21cm profiles towards these stars indicates that the OA is a clumpy structure. Considering the beam size of the LAB data (see Kalberla et al. 2005), it is possible that the HD40893 sight line pierces a very low-density region of the OA. For this reason, it would be valuable to obtain follow-up observations of additional distant stars in the general direction of the OA. Oegerle et al. (2000) have searched for OA absorption in *FUSE* spectra of the central star of the planetary nebula K1-16, and the nondetection of the OA toward K1-16 places a similar constraint, $R_G(\text{OA}) > 8.7$ kpc.⁴ K1-16 is particularly useful because this sight line is only 85'' from the H1821+643 sight line, and it also probes the OA at a greater z height than most of the other stellar sight lines.

Second, considering the intermediate-velocity components at negative velocities seen toward H1821+643, we clearly detect these clouds in the spectra of HD207198, HD208440, and HD209339 (this is most easily seen in comparison of the Si II profiles in Figure 9). The velocity centroids and relative line strengths of these features in the stellar sight lines are quite similar, but not identical, to those of the H1821+643 intermediate-velocity lines. The variations of the intermediate-velocity lines from sight line to sight line are not too surprising given

⁴ Oegerle et al. (2000) report a Heliocentric distance of 1.6 kpc to K1-16. We note that Cahn et al. (1992) determined a somewhat lower Heliocentric distance of 1.0 kpc for K1-16. Use of the Cahn et al. distance reduces the Galactocentric distance constraint to $R_G(\text{OA}) > 8.6$ kpc. This change is very small and has no impact on our discussion.

the angular separations between the stars and the QSO. These variations could provide interesting constraints on the nature of these clouds, particularly for the stellar sight lines, which are relatively close in the sky. The velocities of these features suggest that they are affiliated with the Perseus spiral arm, and in principle, these sight lines can be used to probe gas flows affiliated with the Perseus arm. These intermediate-velocity lines are tangential to this paper, so we defer further analysis of the intermediate-velocity clouds to a future study.

5.2. Complex G

We have found two stars that place upper limits on the distance to Complex G: BD +35 4258 and HD210809. The interstellar C II λ 1334.53 and Si III λ 1206.50 absorption profiles recorded in the STIS echelle spectra of these two stars are shown in Figures 11 and 12, respectively, and the Galactic coordinates and distances of these stars are listed in Table 4. In Galactic coordinates, Complex G extends over $79^\circ \lesssim l \lesssim 122^\circ$ and $-19^\circ \lesssim b \lesssim -1^\circ$, and the velocity range of its 21cm emission is $-190 \lesssim v_{\text{LSR}} \lesssim -90$ km s⁻¹ (Kalberla & Haud 2006). Both BD +35 4258 and HD210809 are in the direction of this HVC, as shown in Figure 2. From Figures 11 – 12, we see that highly significant C II and Si III absorption lines are detected at Complex G velocities toward both BD +35 4258 and HD210809, and in many of the profiles, multiple components are readily apparent. Si II absorption is also detected at the velocity of Complex G toward both stars, but the Si II lines are weaker. The column densities, velocity centroids, and b -values of these C II, Si II, and Si III lines, determined from the STIS spectra via Voigt-profile fitting (§4), are presented in Table 6. The LAB 21cm spectra in the directions of BD +35 4258 and HD210809 are shown in Figures 13 and 14. Although the 21 cm emission was recorded with a large (35.7') beam and is blended with lower-velocity emission, we nevertheless see correspondence between the 21cm emission and the UV absorption.

It is very likely that the UV absorption lines in Table 6 are affiliated with Complex G, and this indicates that this HVC is relatively nearby (see Table 4). Given the distance bracket on Complex C (Thom et al. 2008; Wakker et al. 2007) and the similarity of the Complex G and Complex C velocities, it is quite possible that these HVCs are related. The Outer Arm appears to be located at a similar Galactocentric radius (see above). To further test the connections between these objects, it would be useful to measure the metallicity of the clouds detected toward BD +35 4258 and HD210809. The UV column densities in Table 6 are well constrained, but the H I column densities must be measured. Given the low metal column densities indicated by the STIS data (Table 6), it might be difficult to detect these clouds in 21 cm emission, but it might be possible to extract $N(\text{H I})$ from archival *FUSE* data or new COS observations.

We note that both BD +35 4258 and HD210809 also show high-velocity absorption lines at *positive* velocities, so one might wonder if the positive and negative high-velocity features are related. There is no significant 21 cm emission evident on the positive-velocity side toward these stars (Figures 13 – 14). Given the difference in the 21 cm emission and the large velocity separation of the

TABLE 5
STELLAR SIGHT LINES TOWARD THE OUTER ARM: PROFILE-FITTING MEASUREMENTS

Sight line	Species	Fitted Lines (Å)	v (LSR) (km s ⁻¹)	b (km s ⁻¹)	$\log [N \text{ (cm}^{-2}\text{)}]$
HD43818	C II	1334.53	-79 ± 1	6 ± 1	13.25 ± 0.01
			-60 ± 1	8 ± 1	13.13 ± 0.04
	Si III	1206.50	-77 ± 1	6 ± 1	12.81 ± 0.11
			-60 ± 2	4 ⁺⁵ ₋₂	11.69 ± 0.23

TABLE 6
STELLAR SIGHT LINES TOWARD COMPLEX G: PROFILE-FITTING MEASUREMENTS

Sight line	Species	Fitted Lines (Å)	v (LSR) (km s ⁻¹)	b (km s ⁻¹)	$\log [N \text{ (cm}^{-2}\text{)}]$
BD+35 4258	C II	1334.53	-148 ± 1	8 ± 2	12.89 ± 0.05
			-110 ± 1	9 ± 1	13.98 ± 0.02
			-90 ± 1	6 ⁺³ ₋₂	12.92 ± 0.11
	Si II	1260.42, 1304.37	-111 ± 1	6 ± 2	12.26 ± 0.12
			-108 ± 5	21 ⁺²⁷ ₋₁₂	11.94 ± 0.29
Si III	1206.50	-148 ± 3	6 ⁺¹² ₋₄	12.05 ± 0.16	
HD210809	C II	1334.53	-104 ± 1	17 ± 2	12.95 ± 0.05
			-129 ± 1	5 ± 1	13.70 ± 0.01
	Si II	1260.42	-129 ± 1	5 ± 1	11.82 ± 0.03
	Si III	1206.50	-162 ± 10	16 ⁺²¹ ₋₉	11.83 ± 0.29
			-146 ± 1	4 ⁺³ ₋₂	11.74 ± 0.26
			-127 ± 1	6 ± 1	12.89 ± 0.04

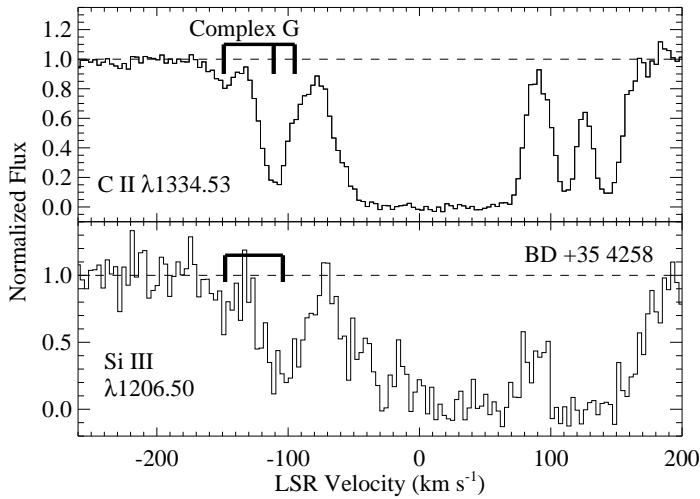


FIG. 11.— Continuum-normalized STIS absorption profiles of the interstellar lines of C II λ 1334.53 (upper panel) and Si III λ 1206.50 (lower panel) observed toward the B0.5 Vn star BD+35 4258, recorded with the E140M echelle mode. The multicomponent absorption lines in the velocity range of HVC Complex G are marked with thick vertical tick marks.

negative- and positive-velocity absorption lines, it is possible that these absorption lines arise in unrelated objects in this general direction. Moreover, a previous study of the nearby star 4 Lac (Bates et al. 1990), which is in the direction of Complex G, detected this positive-velocity gas but not the negative-velocity material. This indicates that the positive-velocity absorption is closer to the Sun (Heliocentric $d < 1.3$ kpc), while the negative-velocity gas is farther away. However, supernova remnants can

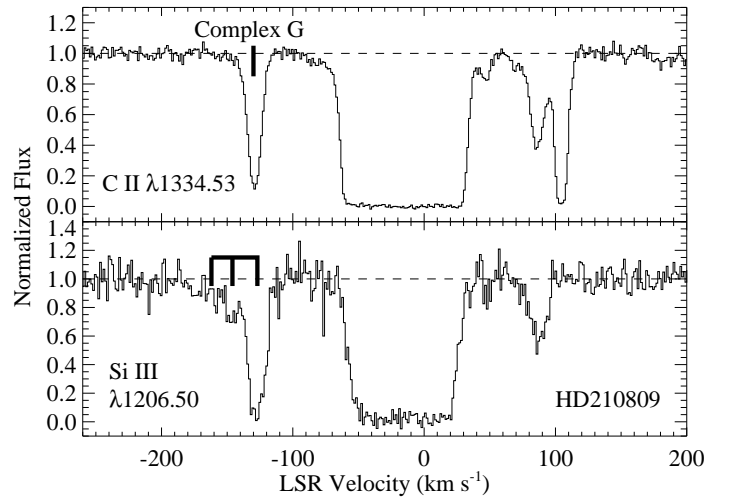


FIG. 12.— Continuum-normalized absorption profiles of the interstellar lines of C II λ 1334.53 (upper panel) and Si III λ 1206.50 (lower panel) observed toward the O9 Iab star HD210809 with STIS in the E140H echelle mode (see Table 1). Highly significant absorption lines at $v \approx -129$ km s⁻¹ (i.e., in the velocity range of HVC Complex G) are marked with thick tick marks.

produce absorption lines with such velocity spreads (e.g., Jenkins et al. 1998; Cha & Sembach 2000), so the nature of the high-velocity absorption lines toward BD +35 4258 and HD210809 deserves further investigation. This is beyond the scope of this paper, so hereafter we will consider our Complex G distance constraint with this caveat in mind.

6. PHYSICAL CONDITIONS AND ABUNDANCES

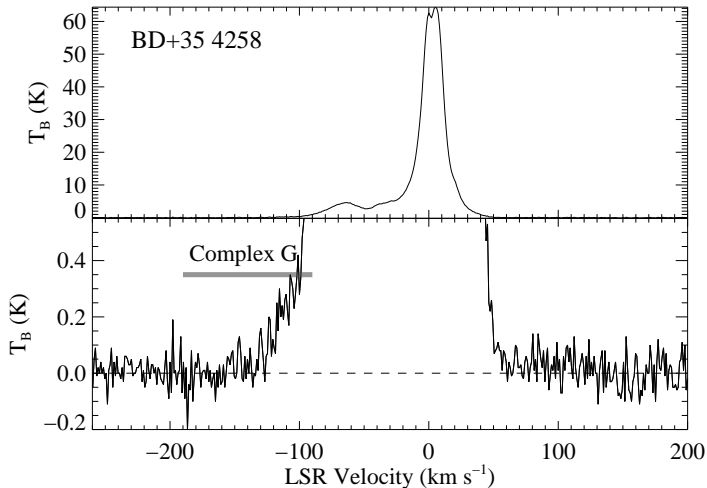


FIG. 13.— H I 21 cm emission in the direction of BD+35 4258 from the LAB Survey (Kalberla et al. 2005). Both panels show the brightness temperature vs. LSR velocity, but the lower panel is zoomed in to more clearly show the 21 cm emission in the velocity range of Complex G (indicated with a thick horizontal bar).

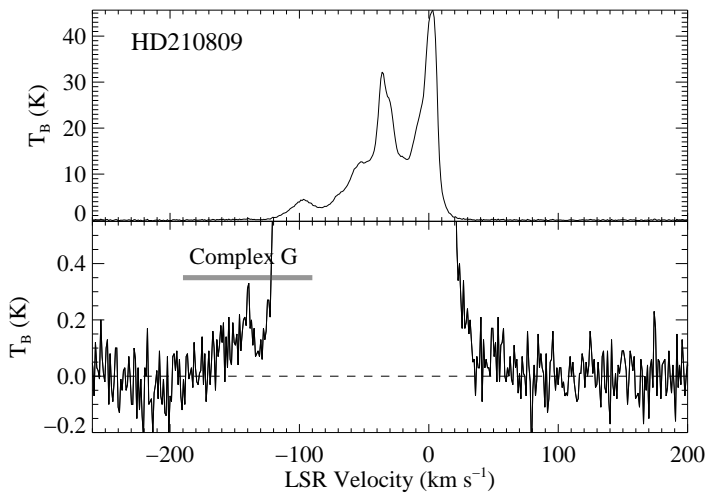


FIG. 14.— H I 21 cm emission in the direction of HD210809 from the LAB Survey, as in Figure 13.

6.1. OA Abundances Toward H1821+643

One of our primary goals in this paper is to measure the gas-phase metallicity of the Outer Arm based on our absorption-line measurements. Toward H1821+643, we are able to measure $N(\text{O I})$, which is highly advantageous because in low-ionization gas, O I is locked to H I by a strong resonant charge-exchange reaction (Field & Steigman 1971). Summing the columns of the three OA components, and adopting the solar abundances from Asplund et al. (2009), we find that the OA oxygen abundance⁵ toward H1821+643 is $[\text{O}/\text{H}] = -0.30^{+0.12}_{-0.27}$, including an allowance for the uncertainty in $N(\text{H I})$ due to the large radio beam (Wakker et al. 2001). In this context, oxygen should be only weakly affected by deple-

⁵ We express abundances in the usual logarithmic notation, $[\text{X}/\text{Y}] = \log(\text{X}/\text{Y}) - \log(\text{X}/\text{Y})_{\odot}$.

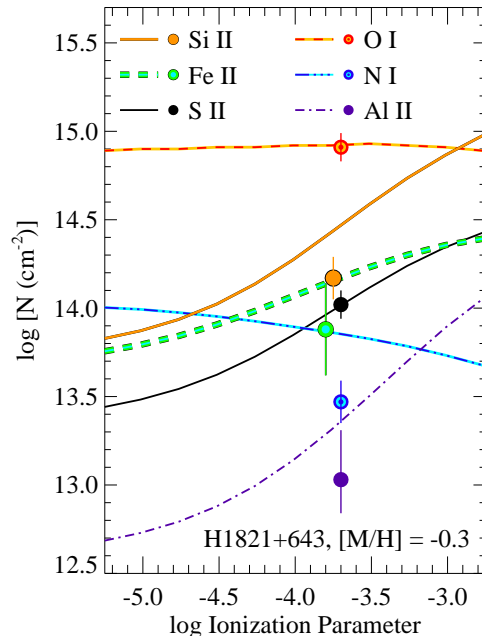


FIG. 15.— Model of gas photoionized by the UV radiation field in the ISM of the Milky Way at a z height of ≈ 0 kpc (i.e., the radiation field in the plane). The radiation field is based on the calculations of Fox et al. (2005, see their Figure 8), and the model assumes that the relative abundances follow the solar pattern, as determined by Asplund et al. (2009). Model column densities are plotted with various curves (see key at the top of the panel) as a function of the ionization parameter U . The Outer Arm column densities observed toward H1821+643 are indicated with filled circles with 1σ error bars, and the different ions are identified by the symbol color coding as indicated in the legend at the top. The observed column densities are plotted at an ionization parameter, $\log U = -3.7$, that fits the observed $N(\text{O I})$ and $N(\text{S II})$ with an overall logarithmic abundance $[\text{M}/\text{H}] = -0.30$. For a few of the observed points, a slight offset was applied to the U position for clarity. As discussed in the text, this model indicates that nitrogen is underabundant and that some dust is present in the gas.

tion onto dust (Savage & Sembach 1996; Jenkins 2009), so this oxygen abundance is a good representation of the overall gas-phase metallicity of the Outer Arm.

Abundances of other elements are more difficult to measure toward H1821+643. The primary problem is that many species can require significant ionization corrections, and it is also possible that some species are depleted onto dust grains. As we will argue below, the OA absorption lines likely arise in cool gas. Therefore the gas is predominantly photoionized, and we can assess ionization corrections using photoionization models. For this purpose, we have the photoionization code CLOUDY (Ferland et al. 1998) to calculate various ion column densities as a function of the ionization parameter U ($=$ ionizing photon density/particle density). In Figure 15 we show the predicted column densities for all of the species that we have detected toward H1821+643 (Table 2), assuming that the gas is photoionized by the ionizing UV flux field in the outer Milky Way as calculated by Fox et al. (2005) with an intensity⁶ of $J_{\nu} = 1 \times 10^{-23} \text{ ergs s}^{-1} \text{ cm}^{-2} \text{ Hz}^{-1} \text{ sr}^{-1}$ at 1 Rydberg.

⁶ The intensity of the ionizing flux at the location of the OA absorption is highly uncertain. However, the photoionization models are homologous in the ionization parameter, so the ionization corrections are insensitive to this uncertainty.

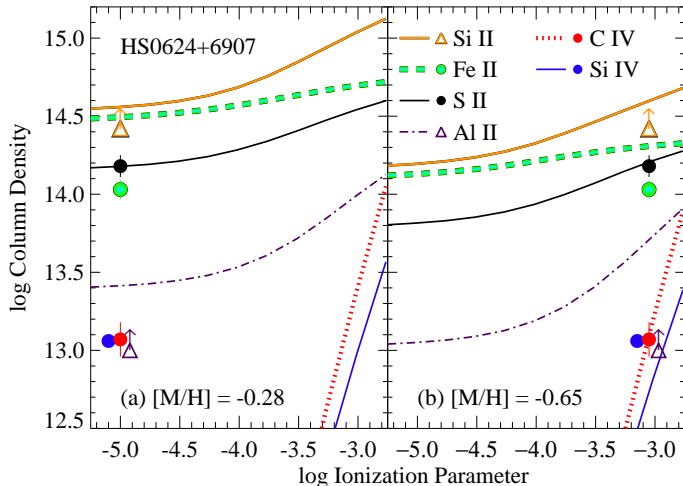


FIG. 16.— Model of gas photoionized by the Galactic UV radiation field at z height = 0 kpc (Fox et al 2005), as in Figure 15, compared to the column densities measured in the Outer Arm toward HS0624+6907. Species that yield reliable column densities are plotted with filled circles with 1σ error bars. Species that have only lower limits on their column densities (due to saturation of all available transitions) are indicated with triangles with upward-pointing arrows. The symbol colors and curve types identify the species as indicated at the top of panel (b). For this sight line, a reliable O I column could not be obtained, so the models are constrained to fit $N(\text{S II})$, and consequently there is some uncertainty in the metallicity of the gas due to ionization corrections. Panel (a) shows a model that provides an upper limit on the metallicity, $[\text{M}/\text{H}] = -0.28$ (at values of U lower than the plotted range, the low-ion curves are flat and thus indicate the same metallicity). Panel (b) plots the observed column densities at the value of the ionization parameter, $\log U = -3.1$, that places a lower limit on metallicity, $[\text{M}/\text{H}] = -0.65$. Increasing the ionization parameter decreases the required metallicity, but the ionization parameter cannot exceed $\log U = -3.1$ because then the model would predict C IV and Si IV columns that exceed the observed values.

As expected, $N(\text{O I})$ is flat over the plotted U range in Figure 15 because it tracks H I precisely as the gas ionization changes, but the columns of other species, with the exception of N I, increase as the gas becomes more ionized because those ions can remain present in ionized gas that contains very little H I. N I behaves like O I and is coupled to the H I, but the N I – H I coupling is weaker.

We can roughly constrain the ionization parameter of the gas by requiring the model to match the observed columns of the species that are lightly depleted by dust, O I and S II. The O I/S II ratio indicates that $\log U \approx -3.7$. At this value of U , the model $N(\text{N I})$ is 0.5 dex higher than the observed N I column. In fact, the observed N I cannot be reconciled with this model at all because this would require a high value of U , and, as can be seen from Figure 15, this would cause the model to predict unacceptably high column densities of S II, Al II, and Fe II; such a model is ruled out by the measured column densities of these species. This high- U model would also produce far more Si IV and C IV than is observed. We conclude that nitrogen is underabundant. Nitrogen underabundance is also observed in the nearby HVC Complex C (Richter et al. 2001; Tripp et al. 2003; Collins et al. 2007). We also notice from Figure 15 that Si II, Al II, and Fe II are all somewhat overpredicted by the model at this U . These elements are all

prone to depletion by dust, so this could indicate that there is a small amount of dust in the OA which removes some of the Si, Al, and Fe from the gas phase and hence causes the observed columns to be somewhat lower than the model predictions. Alternatively, by choosing a lower model ionization parameter, it is possible to fit the Si II, Al II, and Fe II columns without requiring any dust depletion, but in this case the observed $N(\text{S II})$ would significantly exceed the model S II column (see Figure 15). Such an excess of S II has no obvious explanation; it is more likely that the preferred model with $\log U \approx -3.7$ is correct and there is some depletion of Si, Al, and Fe.

6.2. OA Abundances Toward HS0624+6907

Turning to the HS0624+6907 data, we find that, ironically, the higher H I column creates some difficulties because more of the available metal lines are saturated (§4.2). In addition, the HS0624+6907 data are noisier and cover fewer lines. For this sight line, we must mainly rely on S II to estimate the gas-phase metallicity. This species can exist in ionized as well as neutral gas, so we must consider the impact of ionization on the derived metallicity. Figure 16 shows a photoionization model analogous to the H1821+643 model but adjusted to match the H I column observed toward HS0624+6907. From this figure, we see that the ionization parameter is more loosely constrained in this case. However, we can exclude large ionization parameters because if U is too high, the model will predict Si IV and C IV column densities that exceed the observations. The right panel of Figure 16 shows the maximum ionization parameter allowed by this model without exceeding the observed high-ion columns. The upper limit on the ionization parameter indicates that the ionization corrections for S II cannot be large, and the implied Outer Arm metallicity toward HS0624+6907 is $[\text{M}/\text{H}] > -0.65$, similar to the metallicity obtained from the H1821+643 data. In this case, the Si II column is close to the predicted value while Fe II and Al II are somewhat underabundant and, again, may be modestly depleted by dust. The upper limit on the metallicity is derived from the model shown in the left panel of Figure 16. In this case, as the ionization parameter is decreased, the ionization corrections become negligible and the curves all become flat. In this case, the S II column indicates that the metallicity is $[\text{M}/\text{H}] = -0.28$, very similar to the H1821+643 metallicity, and the iron and aluminum must be moderately depleted.

6.3. Physical Conditions

We noted in §4.1 that the H1821+643 absorption profiles of low ions show clear evidence of three components in the Outer Arm, and two of these components are required to be narrow. In addition, while there is clear correspondence between the low ions and more highly ionized gas traced by Si IV and C IV (see Figures 5, 7, and 8), the Si IV and C IV profile shapes are not identical to those of the low ions. There are consistent offsets between some of the low- and high-ion centroids, and the high ions appear to be broader in the $v_{\text{LSR}} \approx -130$ km s $^{-1}$ component. These characteristics suggest that the Outer Arm gas is in a transitional state. This gas could be interacting with the ambient halo/disk gas of the Milky Way, and this interaction is causing the cloud to fragment and dissipate. It is particularly interesting

that the Si IV and C IV lines indicate low line widths. The line width of the Si IV component at $v_{\text{LSR}} = -150$ km s $^{-1}$ indicates⁷ that the gas temperature $T < 10^{4.4}$ K, and the C IV in this component likewise indicates $T < 10^{4.3}$ K.⁸ These upper limits are well below the temperatures where these species are expected to exist in collisional ionization equilibrium (Gnat & Sternberg 2007). Interestingly, rather narrow C IV and Si IV components are frequently identified in the highest resolution STIS echelle spectra probing interstellar clouds in and near the disk (Lehner et al. 2011). Perhaps the gas is simply photoionized, but Lehner et al. (2011) argue that the narrow and weak C IV and Si IV features do not arise in regions photoionized by nearby hot stars. It is interesting to note that hydrodynamic simulations of a cool gas cloud plunging through a hot halo can create this type of signature. For example, Kwak & Shelton (2010) have found that the turbulent mixing layers on the surface of such a cloud can contain a cool phase that is rich in C IV as well as hotter phases that give rise to species such as O VI. Toward H1821+643, Sembach et al. (2003) report strong O VI at $v = -122$ km s $^{-1}$, with $\log N(\text{O VI}) = 13.87 \pm 0.18$ and $b(\text{O VI}) \approx 22$ km s $^{-1}$. Thus, this scenario of a cold cloud plunging through, and interacting with, an ambient medium seems to be consistent with many characteristics of the OA gas toward H1821+643. In this situation, it is quite possible that the gas is not in ionization equilibrium but rather is in an overionized, relatively cool state. However, due to the strong blending of the components in the current STIS data, the detailed parameters of individual components suffer from substantial uncertainties. It would be valuable to obtain new STIS observations of H1821+643 with the E140H grating (which provides substantially higher spectral resolution) to better constrain the line widths/temperatures and kinematics of the gas.

7. SUMMARY

As we have summarized above, the extended gas cloud known as the Outer Arm is usually considered to be part of the warp in the outer Galaxy and possibly the most distant spiral arm. However, the recent observations of Lehner & Howk (2010) have revealed aspects of the OA that are not expected in this scenario – the OA has a high-velocity component that is inconsistent with Galactic rotation and instead indicates that the OA kinematics are similar to those of Complex C, which is close to the OA in velocity and on the sky. We have presented additional observations that can be used to further probe the nature of the OA. Briefly, we find:

1. Based on ultraviolet absorption lines, we have measured OA abundances in the directions of two QSOs, H1821+643 and HS0624+6907. The OA oxygen abundance in the direction of H1821+643 is $[\text{O}/\text{H}] = -0.30_{-0.27}^{+0.12}$. The metallicity derived

⁷ If the line is predominantly thermally broadened, then the gas temperature is directly related to the component b -value, $T = mb^2/2k$. However, other factors (e.g., turbulence) can contribute to the line broadening, so this temperature estimate should be treated as an upper limit.

⁸ The C IV data are more uncertain due to more severe blending with adjacent components, but the presence of a narrow component is supported by the consistent presence of the sharp edge at $v_{\text{LSR}} \approx -150$ km s $^{-1}$ in both lines of the C IV doublet.

from the HS0624+6907 sight line suggests that the OA could have a range of metallicities in different locations with $Z_{\text{OA}} = 0.2 - 0.5Z_{\odot}$, but the HS0624+6907 metallicity is more uncertain and is consistent with the H1821+643 metallicity when uncertainties are taken into account. The OA metallicity is only marginally higher than the abundances usually measured in Complex C, $Z_{\text{Comp.C}} = 0.1 - 0.3Z_{\odot}$ (e.g., Tripp et al. 2003; Collins et al. 2007; Shull et al. 2011).

2. Both the OA and Complex C are underabundant in nitrogen. This is often interpreted to be an indication that the gas is “chemically young” since nitrogen is synthesized in intermediate-mass stars, and thus more time is required to build up the nitrogen abundance than is required for species such as oxygen that are rapidly produced in Type II supernovae (e.g., Vila Costas & Edmunds 1993; Pettini et al. 1995).
3. High-resolution spectroscopy of several stars in the direction of the OA indicates that the object is at a Galactocentric radius of 9 – 18 kpc. Based on currently available constraints, it is possible that the OA and Complex C are at similar distances. In addition, we have detected the HVC Complex G, which is close to the Outer Arm, in absorption toward two stars. This places Complex G relatively close to the solar Galactocentric radius at $R_G = 8 - 10$ kpc.
4. The OA absorption profiles toward H1821+643 show that the OA is a complex, multiphase entity with several narrow components, including narrow features in the profiles of highly ionized species. This suggests that the OA is, at least in part, interacting with the ambient gas of the Milky Way.

This ensemble of information suggests that the Outer Arm might have a more complicated origin than the usual attribution to the outer warp. This concept has been proposed before: Davies (1972) suggested a connection between the OA and Complex C, which he proposed to be generated by the Large Magellanic Cloud. More recently, Kawata et al. (2003) attempted to model the production of both of these structures by the interaction of a satellite galaxy with the Milky Way. While they found that structures similar to the OA + Complex C could be generated, the absence of the interacting satellite (which they require to have a mass comparable to the LMC) in the expected part of the sky poses a problem for this model. At approximately the same time, the Monoceros Ring structure was discovered (Newberg et al. 2002), and given the similarity of the kinematics and location of the Monoceros Ring to the Outer Arm, it is interesting to ask if these high-velocity gas clouds could be related to the merging satellite that produced the stellar Monoceros Ring. We consider this hypothesis in a future paper.

We thank Martin Weinberg and the anonymous referee for many helpful remarks that significantly improved this paper. Some of the STIS data in this paper were obtained through *HST* program 9184, with financial support from

NASA grant HST GO-9184.08-A. Additional support was provided by NASA ADP grant NNX08AJ44G.

REFERENCES

- Aguirre, A., Hernquist, L., Katz, N., Gardner, J., & Weinberg, D. 2001, *ApJ*, 556, 11
- Aracil, B., Tripp, T. M., Bowen, D. V., et al. 2006, *MNRAS*, 367, 139
- Asplund, M., Grevesse, N., Sauval, A. J., & Scott, P. 2009, *ARA&A*, 47, 481
- Bates, B., Catney, M. G., & Keenan, F. P. 1990, *MNRAS*, 242, 267
- Battisti, A. J., Meiring, J. D., Tripp, T. M., et al. 2012, *ApJ*, in press (arXiv:1110.4557)
- Birnboim, Y., & Dekel, A. 2003, *MNRAS*, 345, 349
- Bowen, D. V., Jenkins, E. B., Tripp, T. M., et al. 2008, *ApJS*, 176, 59
- Bregman, J. N. 1980, *ApJ*, 236, 577
- Burton, W. B., & Moore, R. L. 1979, *AJ*, 84, 189
- Burton, W. B., & te Lintel Hekkert, P. 1986, *A&AS*, 65, 427
- Cahn, J. H., Kaler, J. B., & Stanghellini, L. 1992, *A&AS*, 94, 399
- Cannon, J. M., Skillman, E. D., Sembach, K. R., & Bomans, D. J. 2005, *ApJ*, 618, 247
- Carigi, L., Peimbert, M., Esteban, C., & García-Rojas, J. 2005, *ApJ*, 623
- Cha, A. N., & Sembach, K. R. 2000, *ApJS*, 126, 399
- Chen, H.-W., & Lanzetta, K. M. 2003, *ApJ*, 597, 706
- Chiappini, C., Matteucci, F., & Romano, D. 2001, *ApJ*, 554, 1044
- Collins, J. A., Shull, J. M., & Giroux, M. L. 2007, *ApJ*, 657, 271
- Dame, T. M., & Thaddeus, P. 2011, *ApJ*, 734, 24
- Davies, R. D. 1972, *MNRAS*, 160, 381
- Diplas, A., & Savage, B. D. 1991, *ApJ*, 377, 126
- Ferland, G. J., Korista, K. T., Verner, D. A., et al. 1998, *PASP*, 110, 761
- Field, G. B., & Steigman, G. 1971, *ApJ*, 166, 59
- Fitzpatrick, E. L., & Massa, D. 2005, *AJ*, 129, 1642
- Fitzpatrick, E. L., & Spitzer, L. 1997, *ApJ*, 475, 623
- Fox, A. J., Wakker, B. P., Savage, B. D., et al. 2005, *ApJ*, 630, 332
- Haud, U. 1992, *MNRAS*, 257, 707
- Heiles, C. 1984, *ApJS*, 55, 585
- Hopkins, P. K., & Quataert, E. 2010, *MNRAS*, 407, 1529
- Hsu, W. H., Putman, M. E., Heitsch, F., et al. 2011, *AJ*, 141, 57
- Jenkins, E. B. 2009, *ApJ*, 700, 1299
- Jenkins, E. B., Bowen, D. V., Tripp, T. M., & Sembach, K. R. 2005, *ApJ*, 623, 767
- Jenkins, E. B., Tripp, T. M., Fitzpatrick, E. L., et al. 1998, *ApJ*, 492, L147
- Jenkins, E. B., & Tripp, T. M. 2001, *ApJS*, 137, 297
- Jenkins, E. B., & Tripp, T. M. 2011, *ApJ*, 734, 65
- Kalberla, P. M. W., Burton, W. B., Hartmann, D., et al. 2005, *A&A*, 440, 775
- Kalberla, P. M. W., & Haud, U. 2006, *A&A*, 455, 481
- Katz, N., Kereš, D., Davé, R., & Weinberg, D. H. 2003, in *The IGM/Galaxy Connection: The Distribution of Baryons at z = 0*, ASSL Conf. Proc. v281, eds. J. L. Rosenberg & M. E. Putman, (Dordrecht: Kluwer), 185
- Kaviraj, S., Tan, K.-M., Ellis, R. S., & Silk, J. 2011, *MNRAS*, 411, 2148
- Kawata, D., Thom, C., & Gibson, B. K. 2003, *PASA*, 20, 263
- Kepner, M. 1970, *A&A*, 5, 444
- Kereš, D., Katz, N., Fardal, M., Davé, R., & Weinberg, D. H. 2009, *MNRAS*, 395, 160
- Kereš, D., Katz, N., Weinberg, D. H., & Davé, R. 2005, *MNRAS*, 363, 2
- Kimble, R. A., Woodgate, B. E., Bowers, C. W., et al. 1998, *ApJ*, 492, L83
- Kwak, K., & Shelton, R. L. 2010, *ApJ*, 719, 523
- Lehner, N., & Howk, J. C. 2010, *ApJ*, 709, L138
- Lehner, N., & Howk, J. C. 2011, *Science*, 334, 955
- Lehner, N., Zech, W. F., Howk, J. C., & Savage, B. D. 2011, *ApJ*, 727, 46
- Meiring, J. D., Lauroesch, J. T., Kulkarni, V. P., et al. 2009, *MNRAS*, 397, 2037
- Meiring, J. D., Tripp, T. M., Prochaska, J. X., et al. 2011, *ApJ*, 732, 35
- Moos, H. W., Cash, W. C., Cowie, L. L., et al. 2000, *ApJ*, 538, L1
- Moos, H. W., Sembach, K. R., Vidal-Madjar, A., et al. 2002, *ApJS*, 140, 3
- Moran, S. M., Heckman, T. M., Kauffmann, G., et al. 2012, *ApJ*, in press (arXiv:1112.1084)
- Murray, N., Ménard, B., & Thompson, T. A. 2011, *ApJ*, 735, 66
- Narayanan, A., Savage, B. D., & Wakker, B. P. 2010, *ApJ*, 712, 1443
- Oegerle, W. R., Tripp, T. M., Sembach, K. R., et al. 2000, *ApJ*, 538, L23
- Oppenheimer, B. D., Davé, R., Kereš, D., et al. 2010, *MNRAS*, 406, 2325
- Pettini, M., Lipman, K., & Hunstead, R. W. 1995, *ApJ*, 451, 100
- Prochaska, J. X., Gawiser, E., Wolfe, A. M., et al. 2003, *ApJ*, 595, L9
- Prochaska, J. X., & Hennawi, J. F. 2009, *ApJ*, 690, 1558
- Quillen, A. C., Minchev, I., Bland-Hawthorn, J., & Haywood, M. 2009, *MNRAS*, 397, 1599
- Ramspeck, M., Heber, U., & Moehler, S. 2001, *A&A*, 378, 907
- Rao, S. M., Nestor, D. B., Turnshek, D. A., et al. 2003, *ApJ*, 595, 94
- Reid, M. J., Menten, K. M., Zheng, X. W., et al. 2009, *ApJ*, 700, 137
- Ribaudo, J., Lehner, N., Howk, J. C. et al. 2011, *ApJ*, 743, 207
- Richter, P., Sembach, K. R., Wakker, B. P., et al. 2004, *ApJ*, 559, 318
- Sahnow, D. J., Moos, H. W., Ake, T. B., et al. 2000, *ApJ*, 538, L7
- Savage, B. D. & Sembach, K. R. 1991, *ApJ*, 379, 245
- Savage, B. D. & Sembach, K. R. 1996, *ARA&A*, 34, 279
- Savage, B. D., Sembach, K. R., & Lu, L. M. 1995, *ApJ*, 449, 145
- Savage, B. D., Tripp, T. M., & Lu, L. M. 1998, *AJ*, 115, 436
- Sembach, K. R., Wakker, B. P., Savage, B. D., et al. 2003, *ApJS*, 146, 165
- Shull, J. M., Stevans, M., Danforth, C., et al. 2011, *ApJ*, 739, 105
- Strasser, S. T., Dickey, J. M., Taylor, A. R., et al. 2007, *AJ*, 134, 2252
- Tamanaha, C. M. 1997, *ApJS*, 109, 139
- Thilker, D. A., Bianchi, L., Meurer, G., et al. 2007, *ApJS*, 173, 538
- Thom, C., Peek, J. E. G., Putman, M. E., et al. 2008, *ApJ*, 684, 364
- Tripp, T. M., Giroux, M. L., Stocke, J. T., Tumlinson, J., & Oegerle, W. R. 2001, *ApJ*, 563, 724
- Tripp, T. M., Jenkins, E. B., Williger, G. M., et al. 2002, *ApJ*, 575, 697
- Tripp, T. M., Wakker, B. P., Jenkins, E. B., et al. 2003, *AJ*, 125, 3122
- Tripp, T. M., Jenkins, E. B., Bowen, D. V., et al. 2005, *ApJ*, 619, 714
- Tripp, T. M., Meiring, J. D., Prochaska, J. X., et al. 2011, *Science*, 334, 952
- Tripp, T. M., Savage, B. D., & Jenkins, E. B. 2000, *ApJ*, 534, 1
- Tripp, T. M., Sembach, K. R., Bowen, D. V., et al. 2008, *ApJS*, 177, 39
- Tumlinson, J., Werk, J. K., Thom, C. et al. 2011, *ApJ*, 733, 111
- Vila Costas, M. B., & Edmunds, M. G. 1993, *MNRAS*, 265, 199
- Wakker, B. P. 2001, *ApJS*, 136, 463
- Wakker, B. P., Kalberla, P. M. W., van Woerden, H., et al. 2001, *ApJS*, 136, 537
- Wakker, B. P., Savage, B. D., Sembach, K. R., et al. 2003, *ApJS*, 146, 1
- Wakker, B. P., York, D. G., Howk, J. C., et al. 2007, *ApJ*, 670, L113
- Weaver, H. 1974, in *Galactic Radio Astronomy*, Proc. IAU Symp. 60, eds. F. J. Kerr & S. C. Simonson (Boston: Reidel), 573
- Weinberg, M. D., & Blitz, L. 2006, *ApJ*, 641, L33
- Westerhout, G. 1957, *IAUS*, 4, 29
- Wolfe, A. M., Gawiser, E. & Prochaska, J. X. 2005, *ARA&A*, 43, 861
- Woodgate, B. E., Kimble, R. A., Bowers, C. W., et al. 1998, *PASP*, 110, 1183